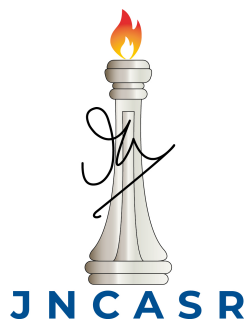


A Study of the Circular Hydraulic Jump: Numerical Simulations and Experiments



Akhilesh Srivastava

Supervisor: Prof. K.R Sreenivas

Engineering Mechanics Unit
Jawaharlal Nehru Centre for Advanced Scientific Research

This dissertation is submitted for the degree of
M.S.(Engg)

April 2025

*To my **Mother**,
for her support and encouragement ...*

Declaration

I hereby declare that the content presented in this thesis entitled "**A Study of the Circular Hydraulic Jump: Numerical Simulations and Experiments** " is the outcome of the numerical and experimental investigations carried out individually at Engineering Mechanics Unit, Jawaharlal Center for Advanced Scientific Research, Bangalore, India under the guidance of **Prof. K.R. Sreenivas**, and has not been submitted elsewhere for the award of any degree or diploma. Acknowledgment and references of other relevant investigations have been added as a general practice in reporting scientific observations.

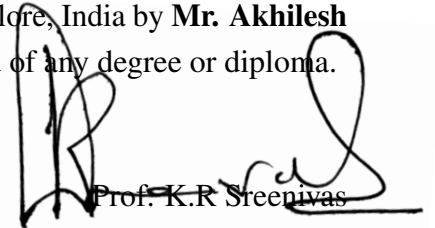


Akhilesh Srivastava

August 2024

Certificate

I hereby certify that the content presented in this thesis entitled "**A Study of the Circular Hydraulic Jump: Numerical Simulations and Experiments** " is the outcome of the numerical and experimental investigations carried out individually at Engineering Mechanics Unit, Jawaharlal Center for Advanced Scientific Research, Bangalore, India by **Mr. Akhilesh Srivastava**, and has not been submitted elsewhere for the award of any degree or diploma.



Prof. K.R. Sreenivas

August 2024

Acknowledgements

I am grateful to **Prof K.R. Sreenivas** for being my mentor and thesis advisor. He has always been very supportive and kind especially when i initiated my research on this topic. I could still remember, our initial meeting while deciding this problem. He asked me whether i knew hydraulic jumps or not, and i was not aware of it. He told me to observe the flow below the faucet which is near the water dispenser at EMU building. After observing, I went back to him and told about the circular pattern and he told me this is your research problem. That was the beginning of my research journey at JNCASR.

The detailed structure of the courses at JNCASR has immensely benefited and has provided a stable ground to stand for my research. In this regard, i would like to thank **Prof. Santosh Ansumali, Prof. Ganesh Subramanian, Prof. Meheboob Alam, Prof. Ajay B. Harish** for all the effort they have put in the coursework.

I want to extent my thanks to **Prof. Diwakar** for teaching me with basics of Finite Volume code which is the method that has been incorporated in my numerical simulation.

My current and previous labmates **Adharsh, Suryadev (the disciplined senior), Manoj, Jishnu and Shubham** for having a fun environment in the lab and their fruitful suggestions (especially by Manoj) during our labmeets.

Apart from the lab, i want to thank **Sangmesh (Professor), Shaumyakant ,Shashank, Anomitra, Ganesh Kumar, Guruprasad, Abhishek, Dr. Pawan, Dr. Abhijeet** for many fruitful discussion over various scientific and non-scientific topics.

Thanks to **Dr. Manojit** for having many wonderful discussions on various aspect of life. He has been a constant source of support and encouragement during my time at JNC. Apart from being a good scientist, he also is a great chef.

Outside EMU, i want to thank **Dr. Momin, Uttam, Mayank, Alok** for all the happy moments in the hostel and helping me with our Sunday lunch party.

And, most importantly, thanks to my parents and Trinath sir for always encouraging me to follow my passion.

Abstract

When a laminar vertical liquid jet hits a horizontal surface, the fluid spreads out radially on the surface. Initially, the spreading film is thin, however as this film spreads radially, at a particular radius (known as the jump-radius) the film thickness abruptly increases, resulting in a phenomenon known as the circular hydraulic jump. There are extensive analytical, numerical, and experimental studies which have explored how various factors, such as flow rate, gravity, viscosity, and surface tension, control the jump-radius. Most earlier studies have indicated a weak dependence of the nozzle radius and the distance from the nozzle to the disk (impinging height; both factors determine the initial momentum flux) on the jump radius.

Vishwanath et al. (2015) specifically conducted experiments and simulations to examine the influence of initial momentum flux on the jump radius. They demonstrated dependence of the jump-radius on the initial momentum-flux through jet nozzle diameter and the impinging height. Here in the present work, building further on this research, we use grid-converged numerical simulations over a broader range of parameters to further investigate the effects of initial momentum flux and the inclination of the impingement surface to the horizontal. Our simulations reveal that increasing the nozzle radius significantly decreases the jump-radius, aligning with the experimental results of Vishwanath et al. (2015). Additionally, inclining the impinging surface affects the flow by providing additional momentum (conversion of potential energy into kinetic energy along the inclined surface) in the spreading direction and reducing the back pressure (due to jump), both of which increase the jump-radius. We conducted numerical simulations with inclinations from 0° to 10° (inclination from 0 to 0.174 radians) to the horizontal. Results indicate that the jump-radius systemically increases with the inclination. Moreover, the jump becomes weaker, as indicated by a lower ratio of pre-jump to post-jump film thickness compared to the horizontal case (0° inclination).

We also performed scaling analysis using a generalized scaling function proposed by Vishwanath et al. (2015), which satisfactorily matched various past experimental results. Although surface tension and disk radius have a weak influence on the jump-radius, they may become significant for smaller jumps, suggesting that our current scaling may need adjustments to account for these effects.

In addition to detailed numerical simulations, we conducted experiments to reconstruct the film thickness variation with radius using a non-invasive, optical technique. For this, we employed the Free-Surface Synthetic Schlieren method developed by Moisy et al. (2009). This technique relies on the apparent displacement of a dotted pattern caused by changes in the refractive index at the interface between two fluids. To validate this method, we reconstructed the profile of a plano-convex lens with known dimensions. We identified a set of optimized parameters that minimized the error based on the absolute difference between the actual and reconstructed profiles. Using these parameters, we successfully reconstructed the free surface profile of a circular hydraulic jump, demonstrating the method as proof of concept.

Table of contents

List of figures	xv
List of tables	xix
Nomenclature	xxi
1 Introduction	1
1.1 Circular Hydrualic Jump	1
1.2 Literature Survey	4
1.3 Objective of this thesis	7
1.4 Structure of Thesis	7
2 Numerical Simulation of Circular Hydraulic Jump	9
2.1 Governing equation	10
2.1.1 VOF description	10
2.1.2 Surface Tension model	12
2.2 Fluid properties	13
2.3 Non-dimensionalization	13
2.4 Normalization of scales	14
2.5 Grid Convergence	15
2.6 Criteria for determining jump radius	17
2.7 Results	17
2.7.1 Effect of Reynolds number	17
2.7.2 Effect of Froude number	19
2.7.3 Effect of Weber number	22
2.7.4 Effect of disk size	23
2.7.5 Effect of initial momentum flux	26
2.7.6 Effect of inclination	30
2.7.7 Scaling plots	32

2.7.8	Conclusion	33
3	Optical reconstruction of free surface profile for circular hydraulic jump	41
3.1	Introduction	41
3.2	DIC Algorithm	42
3.2.1	Problems in DIC	43
3.2.2	Correlation criteria	44
3.3	Error quantifiaction	45
3.4	Experimental Procedure	46
3.4.1	Reconstruction of plano-convex lens	46
3.4.2	Reconstruction of CHJ	49
3.5	Conclusion and Future direction	52
	References	55
	Appendix A Derivation of viscous axisymmetric spread for subcritical region in the circular hydrualic jump	59

List of figures

1.1	Image of circular hydraulic jump in a water dispenser. Water jet hits the solid surface and a sudden increase in film thickness is observed at a fixed radial distance.	1
1.2	Schematic diagram of the hydraulic jump indicating two regions of the flow. Green line demarcates the boundary between inertia dominated region and gravity dominated region, arrows indicate the flow direction.	2
1.3	Analogy between circular hydraulic jump and shock in compressible gases.	3
1.4	Various region in the circular hydraulic jump based on various flow field. . .	3
2.1	Schematic representation of Volume of Fluid method adopted from Haider (2013)	11
2.2	A schematic representation of the physical domain and boundary conditions used for solving the problem.	13
2.3	Variation of film thickness, h , along the radial direction; Numerical simulation has been performed for $Re = 169.1$ and $Fr = 16.81$	16
2.4	Variation of film thickness, H , along the radial direction; Numerical simulation has been performed for $Re = 169.1$ and $Fr = 16.81$; Compared with available experimental and numerical study	16
2.5	Variation of Fr_{local} based on eq 2.20 along the radial direction; Numerical simulation has been performed for $Re = 169.1$ and $Fr = 16.81$; Black dashed line corresponds to location of $Fr_{local} = 1$	18
2.6	Variation of film thickness and radius of jump corresponding to different Reynolds number; Re has been varied in the range of 338.2 to 84.5 by keeping Fr to be 33.74. Nozzle radius of 1.6mm and, height of nozzle ($h_{impingement}$) is 8mm. Red diamond corresponds to the location of $Fr_{local} = 1$ based on eq. 2.20	19

2.7	Variation of film thickness and jump radius by varying initial Fr ; Fr has been varied in the range of 16.87 to 67.48 by keeping Re at 169.10. The nozzle radius was fixed at 1.6 mm and nozzle to disk distance was fixed at 8mm with a disk size of 120mm for all simulations. Red diamond corresponds to the location of $Fr_{local} = 1$ based on eq. 2.20	20
2.8	Schematic of an inviscid flow with a hydraulic jump along with the pressure profile before and after the circular hydraulic jump.	21
2.9	Variation of Fr_{local} ; Fr has been varied in the range of 16.87 to 67.48 by keeping Re at 169.10. The nozzle radius was fixed at 1.6 mm and the impingement height was fixed at 8mm with a disk size of 120mm for all simulations. Red diamond corresponds to the location of $Fr_{local} = 1$ based on eq. 2.20	22
2.10	Effect of Weber Number; Numerical simulations has been performed for surface tension values of 0.01 N/m ,0.02 N/m and 0.04 N/m.	23
2.11	Effect of disk size; Radius of disk has been varied in the range of 70 mm to 200 mm; Re , Fr , and nozzle to disk distance has been kept fixed at 169.10, 16.87, and 8mm respectively. Location the the jump has been marked with red diamond.	25
2.12	Effect of disk size; Radius of disk has been varied in the range of 70 mm to 200 mm; Re , Fr , and nozzle to disk distance has been kept fixed at 169.10, 16.87, and 8mm respectively.	25
2.13	Stagnation flow (Schematic representation) ; Free surface of the jet can be one of the streamlines; Free surface profile is selected based on the jet inlet radius	28
2.14	Effect of initial momentum flux on jump radius; radius of inlet has been varied from 1.6mm to 4.6mm to alter the momentum flux.Flow rate, viscosity, and nozzle to disk distance has been kept fixed to 17ml/s 19mPa-s and 8mm respectively	29
2.15	Effect of initial momentum flux on jump radius.Local Froude number has been monitored by changing the nozzle radii from 1.6mm to 4.6mm.Flow rate, viscosity, and nozzle to disk distance has been kept fixed to 17ml/s 19mPa-s and 8mm respectively	30
2.16	Effect of inclination; Angle of inclination has been varied in the range of 1° to 10° . Numerical simulation has been performed for $Re = 169.10$ and $Fr = 16.87$	31

2.17	Comparison of numerical simulation and experiments by Hansen et al. (1997); Numerical simulations were performed for dimensionless parameter as presented in Table 2.8	34
2.18	Comparison of numerical simulation and experiments with logarithmic correction proposed by Duchesne and Limat (2022); Numerical simulations were performed for dimensionless parameter as presented in Table 2.8	35
2.19	Comparison of numerical simulation and experiments by Vishwanath et al. Vishwanath et al. (2015); Numerical simulations were performed for dimensionless parameter as presented in Table 2.8	36
2.20	Comparison of numerical simulation and experiments by Vishwanath et al. Vishwanath et al. (2015) with logarithmic correction; Numerical simulations were performed for dimensionless parameter as presented in Table 2.8	37
2.21	Comparison of numerical simulations with various inclinations with logarithmic correction ; Numerical simulations were performed for dimensionless parameter as presented in Table 2.8 with inclination variation in range of 1° to 10°	38
2.22	Collapse of non-dimensional jump radius with scaling relation with an inclination factor and logarithmic correction in jump-radius; Numerical simulations were performed for dimensionless parameter as presented in Table 2.8 with inclination variation in range of 1° to 10°	39
3.1	Various types of pattern based on density of random dots; (a) low density random dot pattern; (b) just right density of random dot pattern ($\approx 50\%$ filled area); (c) high density random dot pattern	43
3.2	Flow chart for cross-correlation algorithm.	43
3.3	Flow chart for optical reconstruction.	44
3.4	Aperture problem in image matching; (a) A point on a line can be arbitrarily matched to non-unique points on the displaced line. (b) When the aperture is enlarged to include the endpoints of a line, one could achieve a unique matching.	45
3.5	Various types of error in DIC; (a) Uncertainty in measurement; (b) Discretization error; (c) Total error	46
3.6	Error in the measurement of profile of plano-convex lens as a function of subset size. Three subset size has been chosen and comparison with the actual profile is depicted	47
3.7	Schematic representation of experimental setup	48

3.8	Free surface profile along with gradient of height profile and error in estimation of reconstructed height profile	49
3.9	Error obtained in the reconstructed profile of plano-convex lens according to eq 3.5.	49
3.10	Comparison of gradient obtained by optical reconstruction to the CAD profile	49
3.11	Free surface error in the estimation of reconstructed height profile compared with the actual profile obtained by CAD file.	50
3.12	Schematic of various region in liquid film; Growth of the viscous boundary layer begin at the center of impingement and touches the free surface at the radius r_0	52
3.13	Set of images for performing Digital image correlation of circular hydraulic jump; Experiment was performed at a flow rate of 60 LPH with nozzle diameter of 10 mm and height of impingement to be 100 mm	53
3.14	Optically reconstructed free surface profile for circular hydraulic jump. Flow rate of 45,60, and 90 LPH was maintained with a nozzle radius of 9 mm and disk to nozzle distance of 50 mm.	53

List of tables

2.1	Grid convergence results	15
2.2	Simulation parameter for flow rate variation; viscosity has been varied from 19mPa-s to 76mPa-s, flow rate is fixed at 34ml/s, nozzle radius is 1.6 mm, and nozzle to disc distance is 8 mm	19
2.3	Effect of We on radius of jump; Surface tension values has been taken as 0.01 N/m, 0.02 N/m and 0.04N/m, nozzle radius is 1.6 mm and nozzle to disc distance is 8 mm, $Re = 169.1$ $Fr = 16.87$	24
2.4	Effect of disk size on jump radius; Radius of disk has been varied in the range of 70 mm to 200 mm. Jump radius was found to be decreasing with an increase in disk size. $Re = 169.10$, $Fr = 16.81$, Nozzle radius is 1.6 mm and nozzle to disc distance is 8 mm is kept constant for all simulations	26
2.5	Effect of disk size on post jump film thickness; Radius of disk has been varied in the range of 70 mm to 200 mm. Jump radius was found to be decreasing with increase in disk size. $Re = 169.10$, $Fr = 16.81$, Nozzle radius is 1.6 mm and nozzle to disc distance is 8 mm is kept constant for all simulations	26
2.6	A Comparison between exponent of jet inlet radius for various studies; A non-zero exponent of jet radius proves the dependence of initial momentum flux on the jump-radius	28
2.7	Comparison of jump radius for various nozzle radii for flow rate of 17 ml/s, dynamic viscosity of 19 mPa-s, nozzle to disk distance is 8 mm and disc radius is 120 mm.	29
2.8	Definition and ranges for various simulation parameter.	32

Nomenclature

Acronyms / Abbreviations

α	Volume fraction
F_{br}	Body force in radial direction (N/m^3)
F_{bx}	Body force in axial direction (N/m^3)
Fr	Froude number
Fr_{local}	Local Froude number
g	Acceleration due to gravity (m^2/s)
∇	Gradient operator
h_j	Film thickness at jump location (m)
H_{edge}	Film thickness at the edge of plate (m)
$h_{impingement}$	Nozzle to disk distance (m)
h_{local}	Local film thickness (m)
r_{edge}	Radial distance from jump to edge of disk (m)
Ma	Mach number
μ	Dynamics viscosity ($Pa - s$)
ν	Kinematic viscosity (m^2/s)
p	Pressure (N/m^2)
Q	Flow rate (m^3/s)

r	radial coordinate (m)
Re	Reynolds number
ρ	Density (kg/m^3)
r_{in}	Jet inlet radius (m)
Re_j	Radius of jump (m)
σ	Surface tension (N/m)
t	Time (s)
θ	Angle of inclination from the horizontal (θ)
u_{in}	Jet inlet velocity (m/s)
U_{avg}	average velocity (m/s)
v_r	radial velocity (m/s)
v_x	axial velocity (m/s)
We	Weber number
x	axial coordinate (m)

Chapter 1

Introduction

1.1 Circular Hydraulic Jump

When a laminar liquid jet impinges on a horizontal surface, the liquid initially spreads out as a thin film. At a specific radial distance (the jump-radius), the film-thickness suddenly increases, creating a phenomenon called the circular hydraulic jump. This effect is commonly seen in kitchen sinks when the faucet is turned on: the water jet from the faucet strikes the sink surface, and at a certain distance from the impact point, a circular pattern is observed (see fig 1.1), indicating formation of circular hydraulic jump.



Fig. 1.1 Image of circular hydraulic jump in a water dispenser. Water jet hits the solid surface and a sudden increase in film thickness is observed at a fixed radial distance.

The flow field in this phenomenon consists of two distinct regions: the inertial-dominated region (thin film flow, before the jump) and the gravity-dominated region (after the jump; see fig 1.2).

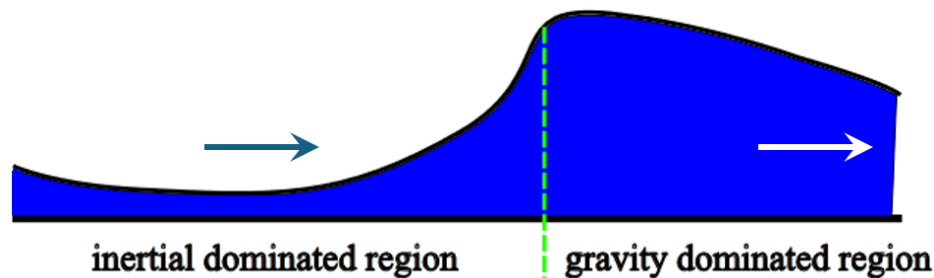
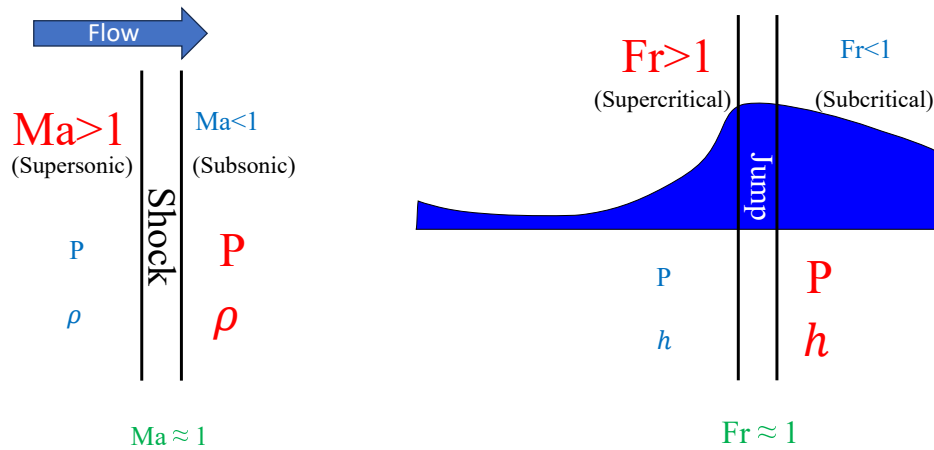


Fig. 1.2 Schematic diagram of the hydraulic jump indicating two regions of the flow. Green line demarcates the boundary between inertia dominated region and gravity dominated region, arrows indicate the flow direction.

The inertia-dominated region consists of a thin, fast-moving liquid layer where the liquid speed exceeds the shallow water wave speed. As a result, disturbances or waves in this region cannot propagate upstream and are carried only downstream. This condition is known as supercritical flow (Froude number greater than one). The second key region is the gravity-dominated region downstream of the jump. In this area, flow velocities are lower, and the film thickness is significantly higher. Due to these factors, the flow speed is slower than the shallow water wave speed, resulting in subcritical flow. In subcritical flow, perturbations can travel in both directions (upstream and downstream), with the Froude number being less than one. Both regions are connected by a sudden increase in film thickness at a specific radial distance from the point of impingement, known as the jump-radius. This hydraulic jump feature resembles a shock in compressible gas flow (see fig 1.3 and 1.4).

- Region A : This region comprises of the stagnation zone which scales with size of impinging jet diameter. In this region, axial velocity of jet changes to radial velocity of the thin film with a constant boundary layer thickness.
- Region B : Outside the stagnation zone, growing boundary layer and inviscid flow coexists together. The velocity profile in this region can be approximated as to be Blasius type boundary layer.
- Region C : The growing boundary layer get connected to the free surface of thin film. In this region, viscous effects are felt in the complete thin film. Moreover, velocity profile changes from the Blasius boundary layer to the self-similar velocity profile.



$$Ma = \frac{\text{Flow speed}}{\text{sound speed}}$$

$$Fr = \frac{\text{flow speed}}{\text{shallow water wave speed}}$$

Fig. 1.3 Analogy between circular hydraulic jump and shock in compressible gases.

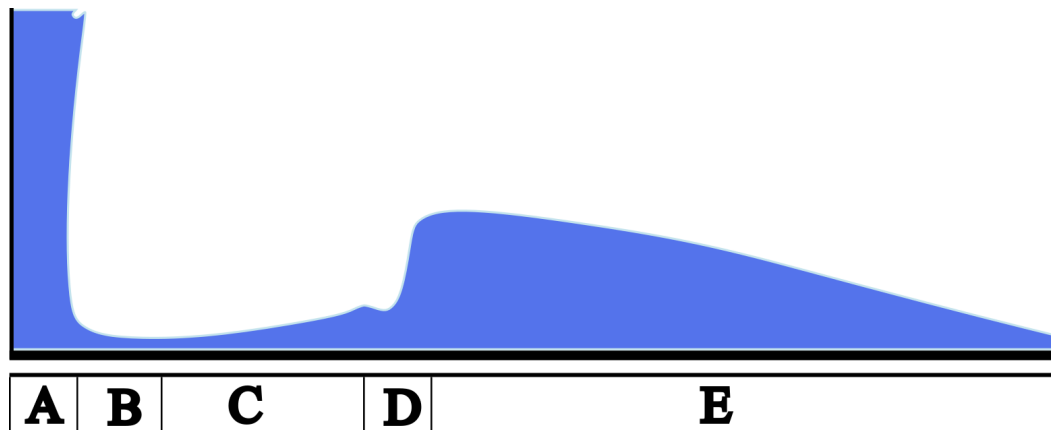


Fig. 1.4 Various region in the circular hydraulic jump based on various flow field.

- Region D : In this region, thin film experiences a sudden increase in the film thickness. This transition lead to a circular hydraulic jump.
- Region E : After the jump, the flow becomes thick and slow making it subcritical. The flow in this region is driven due to the hydrostatic pressure, this is generated due to the sudden increase in film thickness at the location of jump.

Due to the complex flow physics in each region of the circular hydraulic jump, achieving a complete theoretical description is challenging. Additionally, the finite size of the impinging surface makes the problem ill-posed at the edge of the plate, however, the edge condition significantly influence the jump location. The dynamic interplay of various forces is crucial

in determining the origin of the circular hydraulic jump, making its study particularly interesting.

In industrial settings, applications such as jet impingement cooling are widely used due to their high heat transfer efficiency (Liu et al., 1991). Furthermore, the inertial thin film flow generates high shear stress at the walls, which effectively removes viscous layers and scaling from substrates (Yeckel and Middleman, 1987). However, both heat transfer and wall shear stress are significantly impacted by the formation of circular hydraulic jumps.

The next section presents a brief literature survey on circular hydraulic jumps.

1.2 Literature Survey

There have been several attempts to understand the factors affecting the jump radius as well as the origin of the circular hydraulic jump.

- The earliest observation by Rayleigh (1914) identified a circular standing wave when a free jet of water fell on a Petri dish.
- Tani (1949) suggested that flow separation causes the sudden increase in film thickness, leading to the hydraulic jump. They performed a theoretical analysis of the boundary layer equation, including gravity effects, and used a velocity profile ansatz to derive an ordinary differential equation relating film thickness growth to radial spread.
- Watson (1964) solved the laminar and turbulent circular hydraulic jump by analyzing the boundary layer equation without gravity effects. He derived self-similar velocity profiles for radial distances much greater than the jet radius and applied the principle of momentum to determine the jump-radius, assuming a discontinuous height profile without considering the jump width. His analysis works well for larger jumps but not for smaller ones (3 to 4 times the jet radius).
- Craik et al. (1981) conducted experiments and found flow separation as the cause of the hydraulic jump. He noted that instability at the circular jump front increases with downstream film thickness, which he attributed to the reduction in the recirculatory eddy size. These undulations dissipate excess energy at the circular front as gravity waves.
- Bohr et al. (1993) derived a scaling relation for jump-radius by connecting inner and outer solutions of the shallow water equation, including viscosity, as $R_j \sim Q^{5/8} \nu^{-3/8} g^{-1/8}$. This analysis was limited to laminar flow states with low flow

rates and stationary circular hydraulic jumps. The detailed jump structure, such as flow separation, is not captured, and the lack of an asymptotic solution for large radial distances is noted.

- Bush and Aristoff (2003) performed a theoretical analysis to understand the role of surface tension in laminar circular hydraulic jumps. They found surface tension effects to be small in laboratory settings but crucial for smaller jumps (3 to 4 times the jet radius), microgravity conditions, and internal hydraulic jumps between immiscible liquids of comparable density. They provided corrections to Watson's expressions for jump radius, resulting in better scaling for smaller jumps.
- Bush et al. (2006) experimentally observed the emergence of steady polygonal jumps, including patterns like cat's eyes, three- or four-leaf clovers, bowties, and butterflies, attributing these shapes to capillary instability.
- Kasimov (2008) theoretically analyzed shallow water equations obtained by depth-averaging the Navier-Stokes equations on a finite-sized disk. Surface tension effects were included, highlighting their importance in incorporating unsteadiness at the jump front. An increase in surface tension can transition a circular front to non-circular (polygonal) shapes.
- Duchesne et al. (2014) experimentally showed a constant Froude number post-jump, independent of flow rate, viscosity, and surface tension. They proposed a logarithmic correction to Bohr et al.'s (1993) scaling relation, incorporating the finite disk radius effect. Surface tension effects were found negligible for the experimental parameters.
- Experimental and numerical simulations by Vishwanath et al. (2015) established the role of initial momentum flux on jump-radius. By varying nozzle diameter and impingement height, they developed a scaling based on momentum flux and energy dissipation, collapsing a large set of experimental and numerical data. Surface tension effects were not included in the simulation or scaling for jump radius.
- Bhagat et al. (2018) attributed the origin of the circular hydraulic jump to energy losses due to surface tension forces in the expanding liquid sheet. They argued that momentum in the thin liquid film at the jump location is balanced by surface tension and viscous forces alone. Experiments on flat surfaces with various orientations showed no change in jump radius, suggesting gravity is not prominent in selecting the jump radius for expanding hydraulic jumps. They proposed $We^{-1} + Fr^{-2} = 1$ as the condition for determining the jump location. However, they mention that once the

liquid film reaches the edge of the finite disk, a different set of boundary conditions is imposed on the flow, this weakens the role of surface tension on jump-radius.

- Wang and Khayat (2019) developed a theoretical model to predict the height and location of circular hydraulic jumps for high-viscosity liquids, finding gravity crucial in determining jump-radius. Including gravity in the thin-film equation aligned the jump location with singularity, enabling jump-radius determination without prior knowledge of downstream boundary conditions.
- Fernandez-Feria et al. (2019) used three mathematical frameworks—shallow water equation without surface tension, a depth-average model for the shallow water equation with a parabolic velocity profile, and solutions of the full Navier-Stokes equations considering surface tension. The radius of the jump and upstream flow structure from Navier-Stokes simulations matched shallow water equation results for various flow rates, liquid properties, and downstream boundary conditions, showing practical independence from surface tension effects. The downstream flow structure varied due to surface tension effects, identifying a critical surface tension value above which no axisymmetric jump occurred.
- Bhagat and Linden (2020) theoretically analyzed circular hydraulic jumps based on momentum conservation for the radial and wall-normal flow directions on an infinite surface (expanding hydraulic jumps). Applying momentum conservation in the wall-normal direction at a finite radius revealed a singular film curvature, coinciding with the hydraulic jump location determined by a critical Weber number.
- Wang and Khayat (2021) numerically established the roles of surface tension and gravity for water (low viscosity, high surface tension) and silicone oil (high viscosity, low surface tension). Simulations without surface tension and gravity showed that for water, jumps do not occur without surface tension, whereas for silicone oil, jumps occur with either surface tension or gravity activated.
- Ipatova et al. (2021) theoretically studied axisymmetric viscous flow on a rotating disk, analyzing the viscous shallow water equation with inertia, gravity, centrifugal, Coriolis, and surface tension forces. They found that increasing angular velocity causes the jump to vanish in the absence of surface tension effects.
- Zhou and Prosperetti (2022) developed a scaling correlation for the circular hydraulic jump radius on a cone surface based on flow rate, viscosity, gravity, and inclination angle. They created a reduced-order time-dependent hyperbolic model, predicting

the weakening and disappearance of the circular hydraulic jump on a cone's surface. Surface tension dependence was found to be weak in determining the jump radius. Simulations included pulsating jets hitting a flat surface and steady jets on the underside of a cone.

- Wang et al. (2023) divided thin film domains based on the relative strength of gravity and used a composite mean-field approach to understand the circular hydraulic jump. They found that flow in the supercritical region was unaffected by gravity changes but was greatly influenced by viscosity. They also noted that the presence of recirculation does not necessitate a jump.

Thus the set of study presented reflects various attempts to understand the factors affecting the jump radius and the origin of the circular hydraulic jump. Early studies, like those by Rayleigh (1914) reported the phenomenon and Tani (1949), identified key elements such as flow separation as the cause. Subsequent research by Watson (1964) and others provided theoretical and experimental insights, highlighting the roles of surface tension, gravity, and viscosity in shaping the hydraulic jump. Recent studies have further refined these models, examining the effects of momentum flux, high viscosity of liquids, and complex flow dynamics using advanced simulations. Collectively, these efforts have advanced our understanding of the circular hydraulic jump, revealing it to be a phenomenon influenced by a delicate interplay of multiple conditions and parameters.

1.3 Objective of this thesis

Based on the literature mentioned above, we seek to answer some of the relevant fundamental questions :

- What is the role of initial momentum flux in determining the jump radius?
- What is the role of inclination on the location of the circular hydraulic jump?
- How can we reconstruct the free surface profile of the circular hydraulic jump using a non-invasive technique?

1.4 Structure of Thesis

- **Chapter 1** provides a basic introduction to the phenomena of circular hydraulic jump. In this chapter, various important regions in the flow field are described along with a

brief literature survey. Some important questions have been stated as the objective of the thesis in this section.

- **Chapter 2** contains a comprehensive numerical study of various important factors that are crucial in determining the location of the circular hydraulic jump. A parametric study has been carried out for important non-dimensional parameters. These non-dimensional parameters are derived by the Buckingham-Pi theorem. Along with this, a scaling analysis has been performed to understand the dependence of fluid and geometrical parameters on the jump-radius.
- **Chapter 3** comprises the reconstruction of film thickness profile for circular hydraulic jump using free-surface synthetic Schlieren method developed by Moisy et al. (2009). Validation of the method was performed by reconstructing the free surface profile of a plano-convex lens of known dimensions. The validation step provides us with an optimized set of parameters, which was utilized to reconstruct the free surface profile of the circular hydraulic jump.

Chapter 2

Numerical Simulation of Circular Hydraulic Jump

When a laminar liquid jet strikes a horizontal solid surface, it forms a thin film that spreads radially from the point of impact. At a certain radial distance, the film height suddenly increases, creating a phenomenon known as a circular hydraulic jump. This phenomenon was first observed experimentally by Rayleigh (1914), followed by numerous theoretical, numerical, and experimental studies to understand it. Tani (1949) used boundary layer equations to analyze the system, identifying the jump location near the flow separation point. Later, Watson (1964) analytically solved boundary layer equations without gravity, deriving a self-similar velocity profile for both laminar and turbulent flows. Craik et al. (1981) conducted experiments in a closed container, showing a decrease in jump radius with increasing post-jump liquid levels, eventually leading to the jump's disappearance.

In this chapter, we present results from numerical simulations of the circular hydraulic jump, illustrating the variation of film thickness along the radial direction by varying key non-dimensional numbers that influence the jump location and radius. We also investigate the effect of initial momentum flux on the jump radius, as demonstrated experimentally by Vishwanath et al. (2015), and explore the impact of inclination to the horizontal on the jump-radius. The chapter begins with the Navier-Stokes equation, the governing equation for fluid flow, along with the appropriate boundary conditions. A method to track the liquid-gas interface is described, followed by a section on non-dimensionalization based on Buckingham Pi theorem to assist in parametric studies. Grid convergence and validation with previous numerical and experimental results are reported.

A criterion for determining the jump radius, based on the analogy of the circular hydraulic jump to shocks in compressible gases, is presented. A systematic study of various non-dimensional parameters, including Reynolds number, Froude number, and Weber number, is

conducted. We also report results from varying geometrical parameters such as jet nozzle radius, disk size, and inclination while keeping other parameters constant. To understand the influence of various non-dimensional and geometrical parameters on the jump radius, a scaling analysis is performed.

2.1 Governing equation

Simulations has been performed for axisymmetric domain. The equations for mass and momentum conservation are given by

$$\frac{\partial \rho}{\partial t} + \frac{\partial(\rho v_x)}{\partial x} + \frac{\partial(\rho v_r)}{\partial r} + \frac{\rho v_r}{r} = 0 \quad (2.1)$$

$$\frac{(\partial \rho v_x)}{\partial t} + \frac{1}{r} \frac{\partial(r \rho v_x v_x)}{\partial x} + \frac{1}{r} \frac{\partial(r \rho v_r v_x)}{\partial r} = -\frac{\partial p}{\partial x} + \frac{1}{r} \frac{\partial[r \mu (2 \frac{\partial v_x}{\partial x})]}{\partial x} + \frac{1}{r} \frac{\partial[r \mu (\frac{\partial v_x}{\partial r} + \frac{\partial v_r}{\partial x})]}{\partial r} + F_{b_x} \quad (2.2)$$

$$\frac{(\partial \rho v_r)}{\partial t} + \frac{1}{r} \frac{\partial(r \rho v_x v_r)}{\partial x} + \frac{1}{r} \frac{\partial(r \rho v_r v_r)}{\partial r} = -\frac{\partial p}{\partial r} + \frac{1}{r} \frac{\partial[r \mu (2 \frac{\partial v_r}{\partial r})]}{\partial r} + \frac{1}{r} \frac{\partial[r \mu (\frac{\partial v_x}{\partial r} + \frac{\partial v_r}{\partial x})]}{\partial x} + F_{b_r} \quad (2.3)$$

F_{b_x} and F_{b_r} are body forces in x and r direction respectively. In our numerical simulation $F_{b_x} = -\rho g$ since we have acceleration due to gravity in the negative x direction and $F_{b_r} = 0$. These equations are solved using finite volume formulation for two-phase flow and surface has been tracked by Volume of fluid method (Hirt and Nichols (1981)), presented in the next section.

2.1.1 VOF description

Since the problem of circular hydraulic jump is a multiphase flow problem hence one has to keep track of the interface. There are several approaches in computation fluid dynamics to reconstruct interface and one of the is the Volume of Fluid method (VOF) by Hirt and Nichols (1981) which is based on one fluid model i.e. phases will have the same governing equation and will be identified by an indicator function (volume fraction in our case). The VOF formulation is based on the fact that we have two or more immisible or non-interpenetrating phases, and a phase indicator is introduced which keeps track of the phases present in a computation cell called volume fraction(α). For a computational cell, the sum of volume

fraction of all the phases should sum up to unity.

$$\alpha = \begin{cases} 0, & \text{empty cell} \\ 1, & \text{full cell} \\ 0 < \alpha < 1, & \text{interface} \end{cases} \quad (2.4)$$

0	0	0	0	0	0
0.4	0.3	0	0	0	0
1	0.98	0.4	0	0	0
1	1	0.8	0.1	0	0
1	1	1	0.4	0	0
1	1	1	0.7	0	0
1	1	1	1	0.15	0

Fig. 2.1 Schematic representation of Volume of Fluid method adopted from Haider (2013)

The flow field variable and properties of the participating phase are shared and represent a volume-averaged value if the value of volume fraction(α) is known at each computational cell. The interface between phases is tracked by solving continuity type equation for the volume fraction of participation phases. For q^{th} phase, the equation of continuity reads as

$$\frac{1}{\rho_q} \left[\frac{\partial}{\partial t} (\alpha_q \rho_q) + \nabla \cdot (\alpha_q \rho_q \vec{v}_q) \right] = S_{\alpha_q} + \sum_{p=1}^n (m_{pq} - m_{qp}) \quad (2.5)$$

In the case of two phases say p and q, the volume fraction will only be solved for one of them, and the volume fraction for the other phase will be calculated based on the fact that the sum of volume fraction of phases in a computational cell is unity.

$$\alpha_p + \alpha_q = 1 \quad (2.6)$$

The transport properties(density and viscosity in our simulation) are computed based on the amount of component phases in each control volume. Say α_q is calculated then

$$\rho = \alpha_q \rho_2 + (1 - \alpha_q) \rho_1 \quad (2.7)$$

$$\mu = \alpha_q \mu_2 + (1 - \alpha_q) \mu_1 \quad (2.8)$$

We are using algebraic VOF formulation namely Compressive Interface Capturing Scheme for Arbitrary Meshes (CICSAM) introduced by Ubbink and Issa (1999). This method is capable of reconstructing arbitrarily shaped interfaces on complex computational meshes. Furthermore, this method can deal with large deformation including interface rupture and coalescence. The scheme is derived in a way that there could be no diffusion of interface and is only suitable for sharp fluid interfaces. The formulation requires implicit second-order time stepping.

2.1.2 Surface Tension model

For numerical simulations, we have used the Continuum Surface Force model (CSF) proposed by Brackbill et al. (1992). Modeling of surface tension forces by the CSF method brings an additional source term in the momentum equation. To understand the formulation, let us consider a simplified case of an interface having a constant surface tension (Marangoni effects are neglected) in which case only forces normal to interface are important. The pressure drop across the interface can be formulated in terms of the surface tension coefficient and the radii of curvature in the orthogonal direction to the surface given by the famous ‘Young-Laplace’ equation.

$$\nabla p = \sigma \left(\frac{1}{R_1} + \frac{1}{R_2} \right) \quad (2.9)$$

For our simulations, surface curvature is computed using the local gradient of the scalar field α_q . Say \vec{n} to be the normal to interface then

$$\vec{n} = \nabla \alpha_q \quad (2.10)$$

one could define the curvature as the divergence of the unit vector \hat{n} as $k = \nabla \cdot \hat{n}$ where $\hat{n} = \frac{\vec{n}}{|\vec{n}|}$. The surface tension force is as acted on the surface having a pressure difference across them but this has to be formulated as a body force to incorporate in the momentum equation. Using the divergence theorem, surface force is converted to a body force with the following form

$$F_{vol} = \sigma_{ij} \frac{\rho_k \nabla \alpha_i}{0.5(\rho_i + \rho_j)} \quad (2.11)$$

Resulting set of equations are solved using the student version of a commercial solver. Details of the boundary conditions and grids used for obtaining solution are presenting in following sections.

2.2 Fluid properties

Silicon oil (Working fluid)	
Density(kg/m ³)	950
Dynamic viscosity(Pa-s)	0.019
Air (Ambient fluid)	
Density(kg/m ³)	1.25
Dynamic viscosity(Pa-s)	1.81*10 ⁻⁵

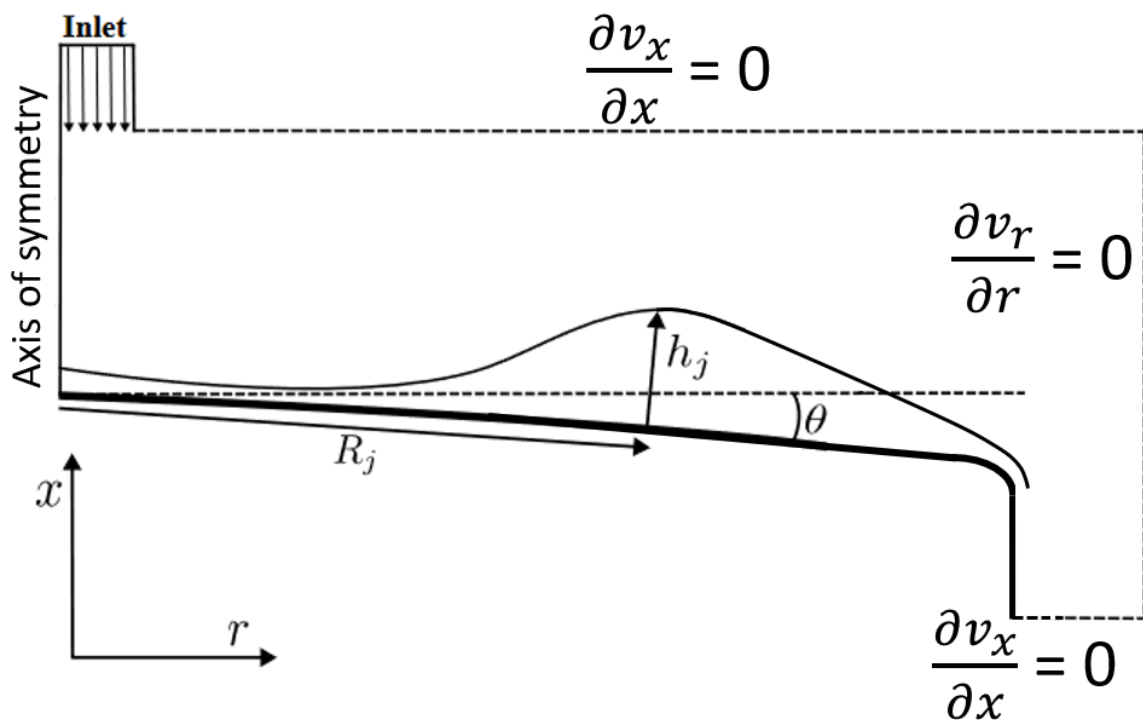


Fig. 2.2 A schematic representation of the physical domain and boundary conditions used for solving the problem.

2.3 Non-dimensionalization

Among the various techniques for finding non-dimensional parameters for a physical fluid dynamics problem, we choose Buckingham pi theorem due to its simplicity. For a physical problem where one dependent parameter is a function of (n-1) independent parameters, a functional dependence can be established of form

$$q_1 = f(q_2, q_3, q_4, \dots, q_{n-1}) \quad (2.12)$$

or

$$g(q_1, q_2, q_3, q_4, \dots, q_n) = 0 \quad (2.13)$$

where the form for f and g is unspecified and they are different from each other. Various non-dimensional π groups can be formed by grouping parameters into a particular form. The number of non-dimensional groups is decided based on the minimum number of dimensions required for characterizing physical parameters involved in experiments(say m).

Note:- for an isothermal fluid flow we require Mass[M], Length[L] and Time[T]. The parameter can be grouped into $(n-m)$ independent π groups which can be expressed as

$$G(\pi_1, \pi_2, \pi_3, \dots, \pi_{n-m}) = 0 \quad (2.14)$$

or

$$\pi_1 = G_1(\pi_2, \pi_3, \pi_4, \dots, \pi_{n-m}) \quad (2.15)$$

To determine the exact functional relation between various π groups one has to perform experiments. Application of the Buckingham-Pi theorem leads us to three non-dimensional quantities. Reynolds number(Re), Froude number(Fr) and non-dimensional jump radius. Length and velocity scales are chosen to be jet inlet radius (r_{in}) and inlet velocity(u_{in}) respectively.

$$Re = \frac{u_{in} r_{in}}{\nu}; \quad Fr = \frac{u_{in}}{(g r_{in})^{1/2}}; \quad \frac{r_j}{r_{in}}$$

2.4 Normalization of scales

Variation of the film thickness along the radial direction is depicted in a normalized sense. The scale to normalize the radial coordinates is the jet inlet radius (r_{in}). However, for the simulation in which there is a change in the radius of the jet, we have presented our results in dimensional form. To normalize the film thickness we have used the nozzle to disk distance or the jet impinging height ($h_{impingement}$) which is fixed for all the simulations.

$$r = \frac{Radius(R)}{r_{in}} \quad (2.16)$$

$$h = \frac{Filmtickness(H)}{h_{impingement}} \quad (2.17)$$

2.5 Grid Convergence

For grid convergence studies, we performed simulations using three different grid sizes (Table 2.1). Local Froude number ($Fr_{local} = Q / (2\pi R H^{1.5} g^{0.5})$) variation along the radius (R) was monitored, the radial location of the jump is where local Fr_{local} falls to unity. In this set of simulations, the properties of the working fluid in the simulation correspond to silicone oil with a density $\rho = 950 \text{ kg/m}^3$, dynamic viscosity $\mu = 19 \text{ mPa}\cdot\text{s}$ and surface tension $\sigma = 0.02 \text{ N/m}$. Ambient fluid was considered to be air with the density $\rho = 1.225 \text{ kg/m}^3$, and dynamic viscosity $\mu = 0.0178 \text{ mPa}\cdot\text{s}$. Nozzle to disk distance was fixed at 8 mm, the disk on which the jet impinges has a radius of 12 cm, and the jet-nozzle radius is fixed at 1.6 mm. Body-fitted square grids were used to discretize the computational domain. As the variation in the jump radius is small ($\sim 3 \%$), when the grid size is halved (table 2.1), we have used 1×10^{-4} size grids in our simulations resulting in 1200 grid points in the radial direction. Moreover, we have compared our results to the relevant experimental and numerical results (Wang and Khayat, 2021, Duchesne et al., 2014) for similar parameters. We also have introduced a small (5 % of disk size) chamfer at the edge of the disk which increases the jump radius by less than 2%. Introducing a chamfer helps the flow to gradually change its flow direction, resulting in the suppression of waves, which were prominent for the sharp edge boundary. With this simple introduction of chamfer at the edge we were able to reduce computational time by 60%.

Table 2.1 Grid convergence results

Grid size(m)	Jump radius(m)	Variation(%)
4×10^{-4}	14.7×10^{-3}	11.36
2×10^{-4}	13.6×10^{-3}	3.03
1×10^{-4}	13.2×10^{-3}	base case

The final set of results is presented with a grid size of 1×10^{-4} (refer Table 2.1).

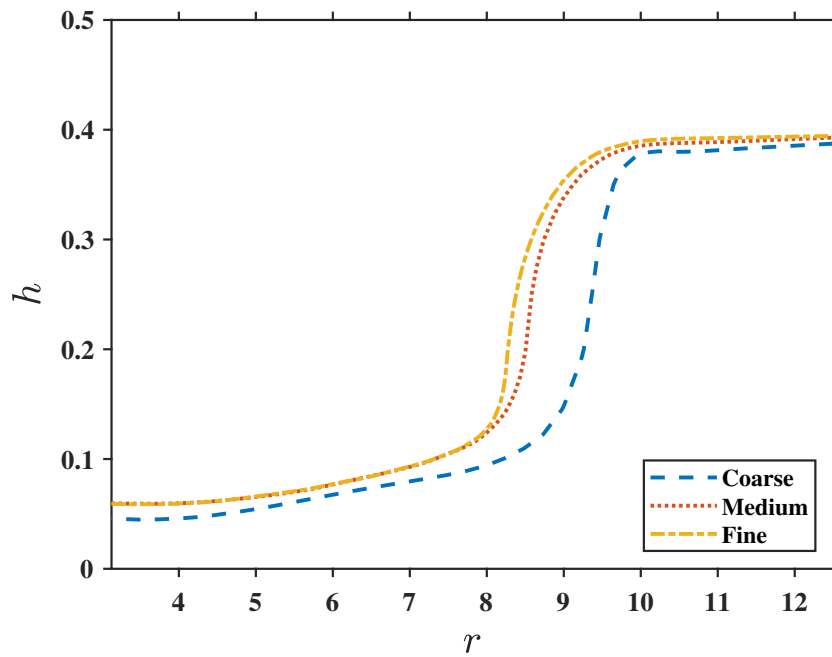


Fig. 2.3 Variation of film thickness, h , along the radial direction; Numerical simulation has been performed for $Re = 169.1$ and $Fr = 16.81$

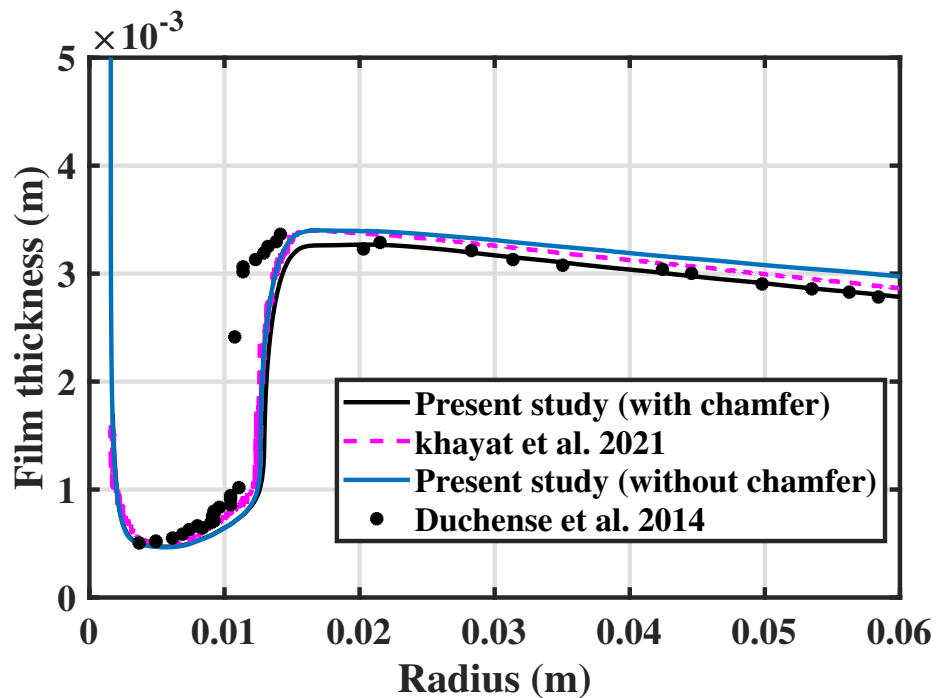


Fig. 2.4 Variation of film thickness, H , along the radial direction; Numerical simulation has been performed for $Re = 169.1$ and $Fr = 16.81$; Compared with available experimental and numerical study

2.6 Criteria for determining jump radius

We have adopted the location of the jump to be the point where the local Froude number (Fr_{local}) approaches unity. This criterion is based on the analogy between the flow behavior of thin inertial liquid film and shocks in compressible gases. Discontinuity in the height profile across the jump could be understood as shocks in liquids (see fig 2.5), which draws its similarity to a discontinuous density field across shocks in gases. The discontinuity divides the flow field into two distinct regions, supersonic and sub-sonic for gases and supercritical and sub-critical for the case of liquid film. In case of gases, this transition occurs at a location where Mach number (Ma) approaches to unity. Similarly we have adopted $Fr_{local} = 1$ as a criterion for transition from supercritical flow to sub-critical flow.

$$Q = 2\pi RHU_{avg} \quad (2.18)$$

$$Fr_{local} = \frac{U_{avg}}{\sqrt{gH}} \quad (2.19)$$

$$Fr_{local} = \frac{Q}{2\pi RH^{1.5}g^{0.5}} \quad (2.20)$$

Here, Q is the flow rate, H is the local film thickness at the radius, R , from the impinging point.

2.7 Results

2.7.1 Effect of Reynolds number

After the jet fluid hits the horizontal surface, it spreads out as a thin film. Initially, the film's free surface is not affected by the no-slip condition at the solid surface below. The viscous boundary layer grows from the point of impingement as the liquid layer continues to spread radially. Eventually, this boundary layer reaches the air-liquid interface at a certain radial distance. Beyond this point, the entire liquid layer experiences viscous effects (Watson (1964)), causing the average velocity in the film to decrease. In the radially spreading film, if the deceleration due to viscosity outweighs the effect of the increased area due to the larger radius, the film thickness starts increasing to maintain mass balance.

The Reynolds number (Re) measures the relative strength of inertia forces compared to viscous forces. By varying Re , we can understand the growth of the boundary layer and the retardation of flow in the thin film. In inviscid fluid flow, a hydraulic jump is impossible without specifying an outer fluid film thickness. Higher Re indicates higher average film

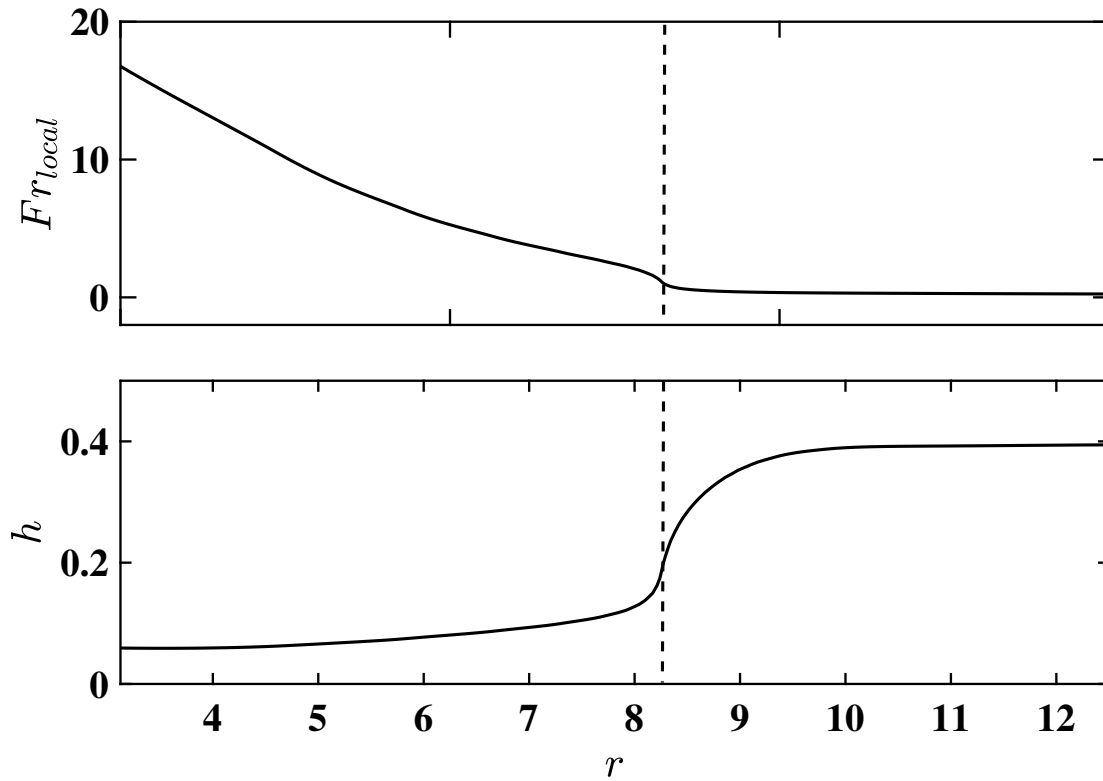


Fig. 2.5 Variation of Fr_{local} based on eq 2.20 along the radial direction; Numerical simulation has been performed for $Re = 169.1$ and $Fr = 16.81$; Black dashed line corresponds to location of $Fr_{local} = 1$

velocity and a thinner viscous boundary layer, slowing the growth of film thickness. In our study, we varied Re by changing the liquid viscosity while keeping other parameters constant. Our results show that increased liquid viscosity leads to a lower jump radius but higher post-jump film thickness for a given flow rate.

As the jump radius decreases, a larger sub-critical region forms for the same disk radius, resulting in a larger volume of fluid to be driven (see fig. 2.6). To support the continuous flow of liquid after the jump, an increase in post-jump film thickness is needed to raise the hydrostatic pressure driving the fluid volume post-jump. Additionally, an increase in film thickness at the disk's edge is observed. These factors contribute to the increase in post-jump film thickness and will be discussed separately in the forthcoming section.

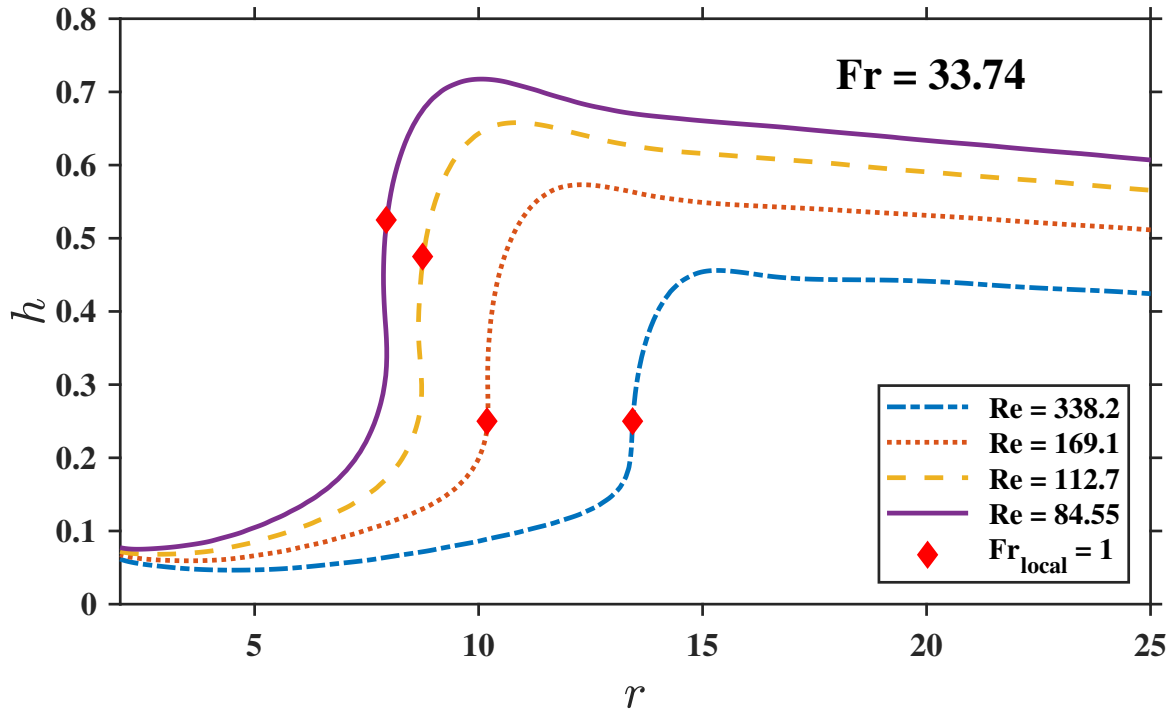


Fig. 2.6 Variation of film thickness and radius of jump corresponding to different Reynolds number; Re has been varied in the range of 338.2 to 84.5 by keeping Fr to be 33.74. Nozzle radius of 1.6mm and, height of nozzle ($h_{impingement}$) is 8mm. Red diamond corresponds to the location of $Fr_{local} = 1$ based on eq. 2.20

Table 2.2 Simulation parameter for flow rate variation; viscosity has been varied from 19mPa-s to 76mPa-s, flow rate is fixed at 34ml/s, nozzle radius is 1.6 mm, and nozzle to disc distance is 8 mm

Re	Fr	R(mm)	r
338.20	33.74	21.5	13.43
169.10	33.74	16.3	10.18
112.73	33.74	14.0	8.75
84.55	33.74	12.7	7.93

2.7.2 Effect of Froude number

The hydraulic jump can be understood as a transition from a supercritical flow to a sub-critical flow. In this section, we monitored the Froude number(Fr) by other parameters fixed, to understand its effect on the film thickness and jump-radius. As reported in figure 2.7, we observe an increase in the jump-radius as well as an increase in post-jump film thickness as we increase the Froude number (Fr). For higher Fr , the fluid flow becomes

more supercritical, as a result, the flow takes a larger radial distance to undergo a transition from supercritical to sub-critical. The delay in the decay of Fr_{local} can be observed in fig 2.9 which is a signature of higher initial Fr , which results in a larger jump radius.

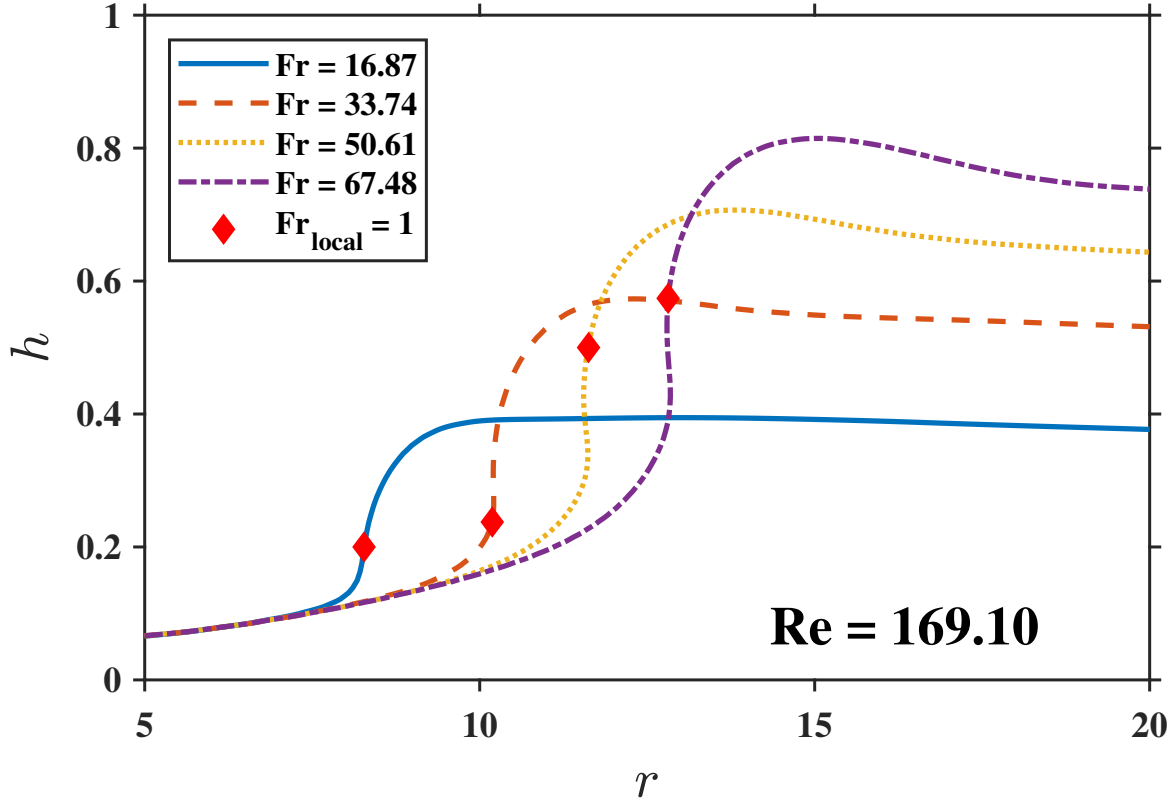


Fig. 2.7 Variation of film thickness and jump radius by varying initial Fr ; Fr has been varied in the range of 16.87 to 67.48 by keeping Re at 169.10. The nozzle radius was fixed at 1.6 mm and nozzle to disc distance was fixed at 8mm with a disk size of 120mm for all simulations. Red diamond corresponds to the location of $Fr_{local} = 1$ based on eq. 2.20

The increase in the post-film thickness can be explained using inviscid arguments as follows. We could obtain a relation between pre-jump and post-jump height by combining continuity of mass and momentum balance (Belanger condition) across the jump.

$$H_1 U_1 = H_2 U_2 = \frac{Q}{2\pi r_j} \quad (2.21)$$

$$\rho Q(U_1 - U_2) = 2\pi r_j H_2 (\rho g H_2) - 2\pi r_j H_1 (\rho g H_1) \quad (2.22)$$

$$\left(\frac{H_2}{H_1}\right)^2 - 1 = Fr_1^2 \left(1 - \frac{U_2}{U_1}\right) \quad (2.23)$$

$$(2.24)$$

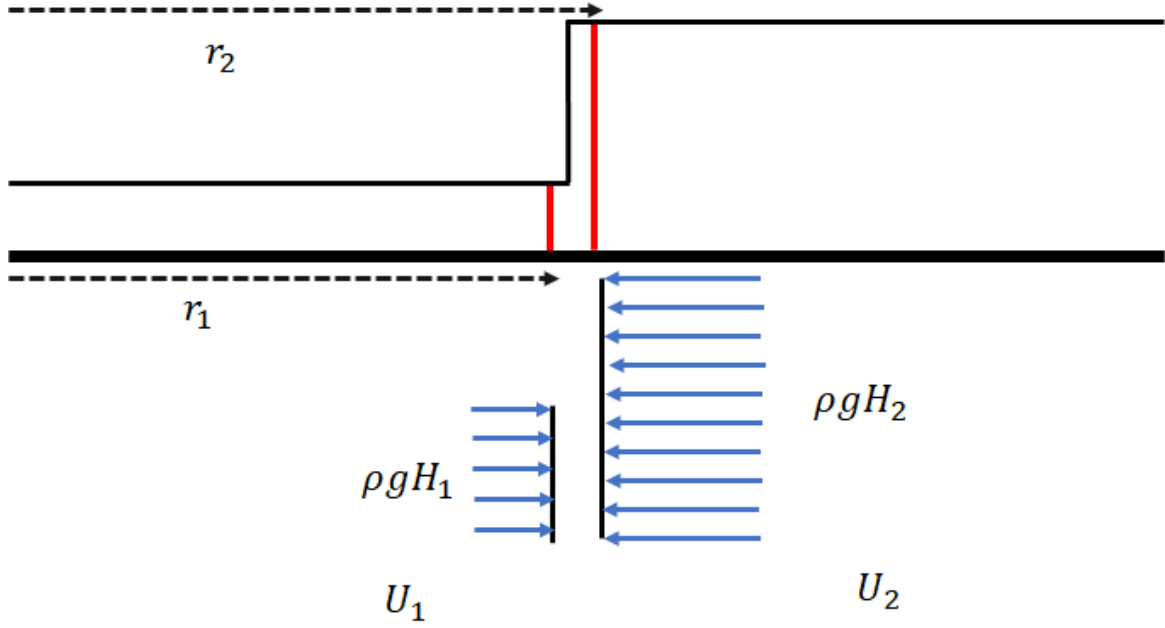


Fig. 2.8 Schematic of an inviscid flow with a hydraulic jump along with the pressure profile before and after the circular hydraulic jump.

since fluid loses most of its momentum after the jump, post-jump velocity is considerably lower than pre-jump velocity. Hence $U_2 \ll U_1$ therefore $\frac{U_2}{U_1} \ll 1$

$$\frac{H_2}{H_1} \propto \sqrt{1 + Fr_1} \quad (2.25)$$

where Fr_1 is defined as $\frac{U_1}{(gH_1)^{0.5}}$. From eq.2.25 we can infer that higher Froude based on pre-jump velocity and film thickness corresponds to higher post-jump film thickness which can explain the variation in fig. 2.7. A similar argument has been earlier presented by Dasgupta (2010).

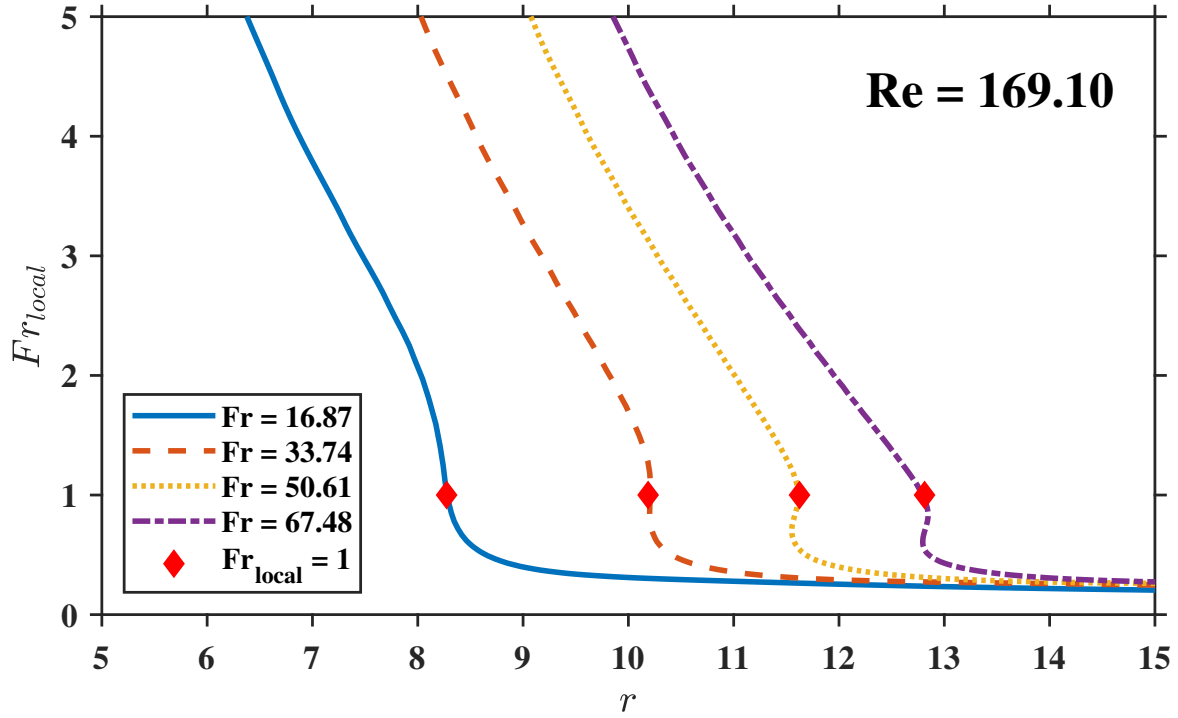


Fig. 2.9 Variation of Fr_{local} ; Fr has been varied in the range of 16.87 to 67.48 by keeping Re at 169.10. The nozzle radius was fixed at 1.6 mm and the impingement height was fixed at 8mm with a disk size of 120mm for all simulations. Red diamond corresponds to the location of $Fr_{local} = 1$ based on eq. 2.20

2.7.3 Effect of Weber number

The role of surface tension in the frontal stability of circular hydraulic jump has been highlighted by various theoretical, numerical, and experimental studies (Kasimov, 2008, Fernandez-Feria et al., 2019, Craik et al., 1981, Bush et al., 2006). In our numerical simulations, we found a stable axisymmetric jump front for the range of parameters mentioned in table 2.8. Weber number (We) accounts for the relative strength of inertia and surface tension forces. We have defined We based on jet inlet velocity and jet inlet radius as:

$$We = \frac{\rho v_{in}^2 r_{in}}{\sigma} \quad (2.26)$$

In figure 2.10 we could observe a transition from shock-like jump to a more gentle smooth hump-like jump. Surface tension can become important for the determination of jump radius in cases of developing circular hydraulic jump (Bhagat et al. (2018), Bhagat and Linden (2020)) where the subcritical developing region after the jump ceases to contribute. However, for the cases of developing jumps, assigning a single value for the jump radius

seems infeasible as it continuously changes with the subsequent development of a gravity-dominated region. Our numerical simulations have been performed till a steady state is reached, this ensures the complete development of both upstream and downstream flow field. Using three different surface tension values (0.01 N/m, 0.02 N/m, and, 0.04 N/m) for our numerical simulations, we found the difference in the jump-radius to be within 2% variation for the case of developed circular hydraulic jump. . As highlighted earlier, one could obtain a steady non-circular hydraulic jump as observed in experiments by Bush et al. (2006). However, in the current thesis, we have considered steady axisymmetrical hydraulic jumps only, and 3-D simulations are kept for future investigations.

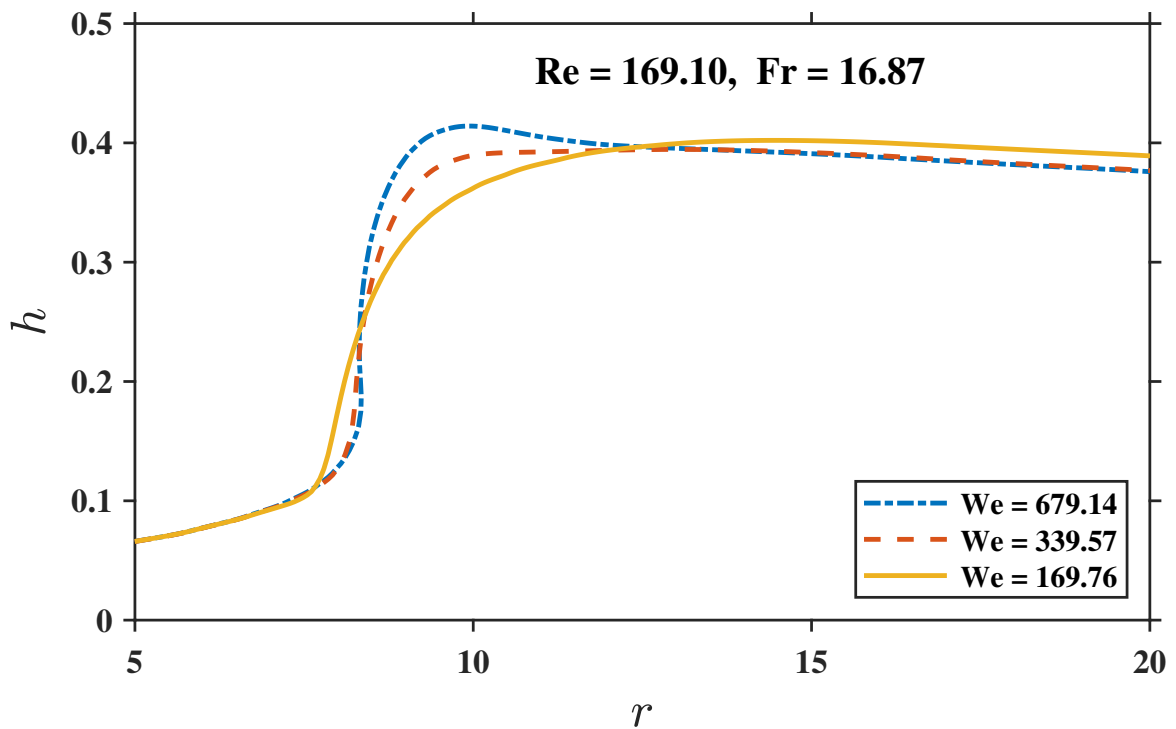


Fig. 2.10 Effect of Weber Number; Numerical simulations has been performed for surface tension values of 0.01 N/m, 0.02 N/m and 0.04 N/m.

2.7.4 Effect of disk size

Experiments performed by Craik et al. (1981) and Ellegaard et al. (1996) showed the effect of an increase in post-jump film thickness on the frontal stability of jump. A transition from type I (single vortex toroidal core) to type II (double vortex toroidal core) jump is observed in their experiments. In our simulation, an increase in the post-jump film thickness is observed for the larger radius of the disk which agrees with the experimental observation mentioned above. This increase can be associated with an increase in the available fluid after the jump

Table 2.3 Effect of We on radius of jump; Surface tension values has been taken as 0.01 N/m, 0.02 N/m and 0.04 N/m, nozzle radius is 1.6 mm and nozzle to disc distance is 8 mm, $Re = 169.1$ $Fr = 16.87$

$\sigma(N/m)$	We	r	$change(\%)$
0.01	679.14	8.3125	(+)0.757
0.02	339.57	8.25	base case(-)
0.04	169.76	8.125	(-)1.515

which needs to be pushed from the edge of the disk. Since the flow after the hydraulic jump is driven predominately by the hydrostatic pressure, a higher amount of pressure is required to drive the flow for a larger radius of disk with a fixed flow rate. Our numerical simulations are performed for the free fall of liquid film at the edge boundary. However, it is observed in experiments by Craik et al. (1981) that post-film thickness continues to increase as they perform the circular hydraulic jump in a closed container. Since there was no way for the liquid to escape from the container, post-jump film thickness kept increasing due to the accumulation of excess liquid after the jump. This resulted in the subsequent decrease in the jump-radius and finally disappearance of the hydraulic jump. Numerical simulations have been performed to understand to effect of disk size on jump radius and film thickness after the jump. Size of the disk is chosen to be 70mm, 120mm(base case geometry), 150mm, and 200mm. Variation in post-jump film thickness was found in the range of 13% and jump radius to be within 7%. The effect of the disk radius on the jump height can be understood by assuming flow after the jump to be within lubrication limits. One could obtain a logarithmic dependence of disk radius on jump height (Bohr et al., 1993, Duchesne et al., 2014, Bhagat and Linden, 2022) as follows

$$H_j = H_{edge} + 6 \frac{\nu Q}{\pi g} \ln\left(\frac{r_{edge}}{r_j}\right) \quad (2.27)$$

where H_j is the film thickness at the jump location, r_{edge} is the distance between jump location and edge of the plate and H_{edge} is the film thickness at the edge of the plate (for derivation see appendix). From the equation 2.27 we can deduce that, an increase in the radius of the disk corresponds to an increase in the film thickness at the jump location. This analysis brings in a new length scale that could be important for the determination of the jump-radius however, for our parametric space we have reported a weak dependence. Note that for the case of variation of Re in section 1.6.1, as we reduce the Re we observe a lower jump-radius but a higher film thickness at jump location. This increase in the post-jump film thickness can be understood as an effective increase in the r_{edge} . Since the jump radius is

small the distance from the location of the jump to the edge of the plate increases for a fixed plate size.

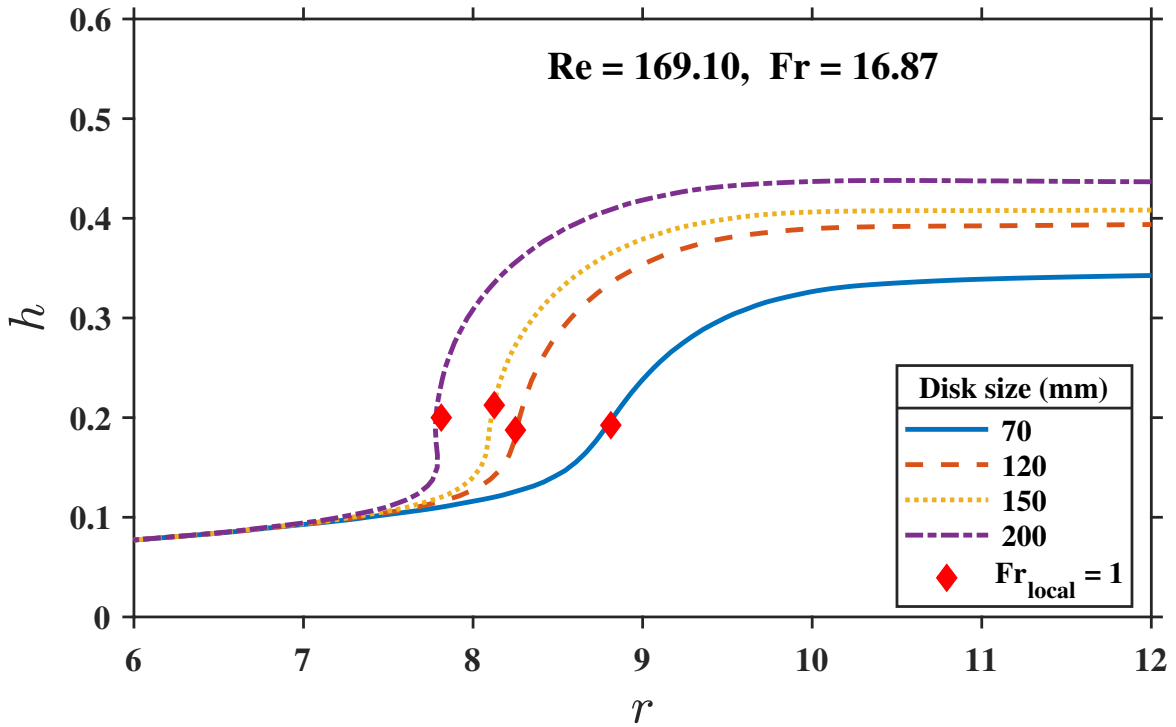


Fig. 2.11 Effect of disk size; Radius of disk has been varied in the range of 70 mm to 200 mm; Re, Fr, and nozzle to disk distance has been kept fixed at 169.10, 16.87, and 8mm respectively. Location the the jump has been marked with red diamond.

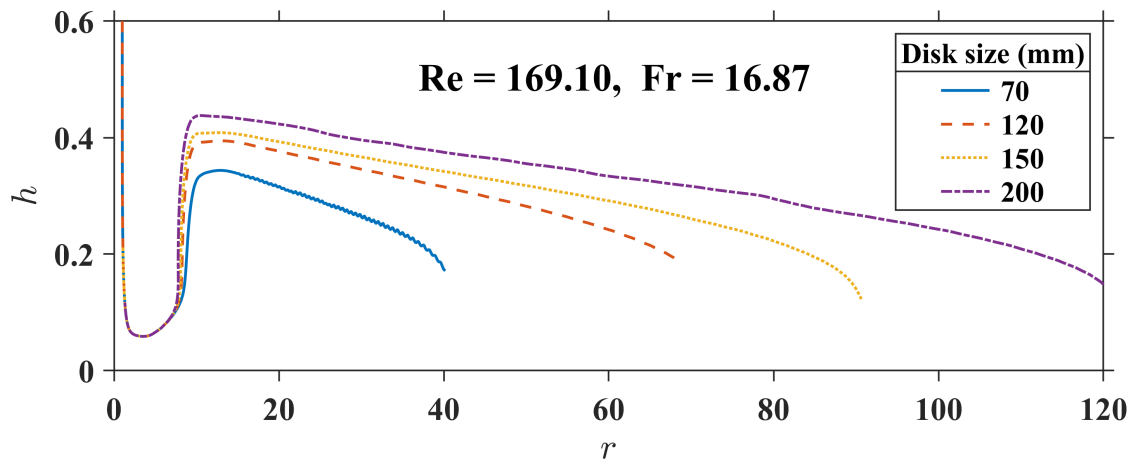


Fig. 2.12 Effect of disk size; Radius of disk has been varied in the range of 70 mm to 200 mm; Re, Fr, and nozzle to disk distance has been kept fixed at 169.10, 16.87, and 8mm respectively.

Table 2.4 Effect of disk size on jump radius; Radius of disk has been varied in the range of 70 mm to 200 mm. Jump radius was found to be decreasing with an increase in disk size. $Re = 169.10$, $Fr = 16.81$, Nozzle radius is 1.6 mm and nozzle to disc distance is 8 mm is kept constant for all simulations

Disk size (mm)	r	Change(%)
70	8.8125	(+)6.8182
120	8.250	base case
150	8.125	(-)1.5152
200	7.8125	(-)5.3030

Table 2.5 Effect of disk size on post jump film thickness; Radius of disk has been varied in the range of 70 mm to 200 mm. Jump radius was found to be decreasing with increase in disk size. $Re = 169.10$, $Fr = 16.81$, Nozzle radius is 1.6 mm and nozzle to disc distance is 8 mm is kept constant for all simulations

Disk size (mm)	h	Change(%)
70	0.3437	(-)12.86
120	0.3945	base case
150	0.4085	(+)3.56
200	0.4379	(+)11.01

2.7.5 Effect of initial momentum flux

Momentum flux is the rate of transport of the momentum per unit time from a fixed region in space. In simplified words, we could understand it as a mechanical quantity that is proportional to the product of the flow rate and velocity normal to the direction of flow across a fixed region in space. As instructive from the definition above, if we want to alter the momentum flux we need to vary the fixed region in space through which the flow is occurring. This idea is pictorially demonstrated by a simplified schematic of a constant head setup with two different-sized nozzles at the bottom. The tank with the smaller nozzle shoots the jet to a larger distance as compared to the other setup with a larger nozzle diameter for a fixed head. In the case of a circular hydraulic jump, this dependence on the nozzle diameter and jet impingement height was systematically explored by Vishwanath et al. (2015). They have numerically and experimentally established the dependence of initial momentum flux. A similar comparison with the scaling of Bohr et al. (1993) has been performed. A non-zero exponential power on the jet inlet radius was found which was in agreement with Vishwanath et al. (2015) which proves the dependence of jet radius on jump-radius (see tab2.6). However,

numerical simulation by Vishwanath et al. (2015) have shown the dependence of initial momentum flux on a smaller parameter range. In continuation, we tried exploring the initial momentum flux effect for a larger parametric space using numerical simulations. We kept the impinging height fixed and adjusted momentum flux by suitably choosing different nozzle radii for a fixed flow rate. Furthermore, to understand the dependence of initial momentum flux on the jump-radius, we have monitored the variation of the Froude number (based on film thickness). A lower nozzle radius corresponds to a higher initial momentum flux for a fixed flow rate which results in a higher jump-radius. This observation in our numerical simulation agrees with the experimental finding of Vishwanath et al. (2015). To understand the effect of the nozzle radii on the initial film thickness, an understanding of the stagnation zone is essential. The spread of the stagnation zone is of the same order as the radius of the jet which was reported previously in several studies (Watson (1964), Wang and Khayat (2019)). Most of the theories that are developed to predict the jump do not consider the effect of the stagnation zone. The initial film thickness after the impingement is a crucial initial condition for determining the jump-radius as the local Froude number at the radial location is solely determined by it. We already have discussed the importance of the local Froude number in selecting the location of the jump (at $r = r_{jump}$ $Fr_{local} \approx 1$). Near the solid wall, the jet turns and forms a thin liquid sheet, while this turning an initial film thickness by the flow is selected. This selection is predominately decided by the jet inlet radius. Jet while turning experiences the surface tension effect (due to curvature) and the effect of the boundary layer in the stagnation zone. Liu and Lienhard (1993) has proved that if We number based on the jet inlet diameter is large, one could expect an free surface profile corresponding to a stagnation point flow. For all of our simulations, We based on inlet jet diameter is $O(100)$ making the surface tension effects weak at the point of impingement. Wang et al. (1989) has analysed the thickness boundary layer in the stagnation zone and found

$$h_{fs} = d_{in} \quad (2.28)$$

$$\delta = 1.98 \left(\frac{\nu}{a} \right)^{0.5} \quad (2.29)$$

$$a = 0.44 \frac{U_0}{r_{in}} \quad (2.30)$$

where h_{fs} is the estimate of the free surface height, U_0 is the average velocity from the jet inlet, and δ is the boundary layer thickness in the stagnation zone. For our numerical simulations, we have considered the mean value of the ratio of the boundary layer and the free surface height. We found the ratio to be 10.46% with a standard variation of 4.55 %. With this, the effect of surface tension and stagnation boundary layer were found to be weak

and one could consider the initial film thickness to be predominately dependent on the jet nozzle radius. Most of the previous experiments have shown a maximum of 10% change in the jump-radius by changing the size of the nozzle (Duchesne et al. (2014)). In contrast, experimental findings by Vishwanath et al. (2015) have shown that in some cases by suitably increasing momentum flux one could almost double the jump-radius. For our numerical simulations, we have found that the jump-radius can have an increase of almost 27% which agree with arguments of Vishwanath et al. (2015).

Exponents	(Vishwanath et al., 2015)	(Bohr et al., 1993)	Present study
a	0.440	0.47076	0.4363
b	0.414	0.375,	0.4078
c	0.322	0.25,	0.3112
1-b-2.5c	-0.219	0	-0.1858

Table 2.6 A Comparison between exponent of jet inlet radius for various studies; A non-zero exponent of jet radius proves the dependence of initial momentum flux on the jump-radius

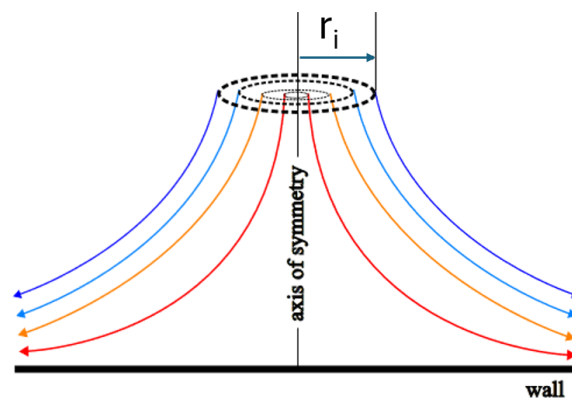


Fig. 2.13 Stagnation flow (Schematic representation) ; Free surface of the jet can be one of the streamlines; Free surface profile is selected based on the jet inlet radius

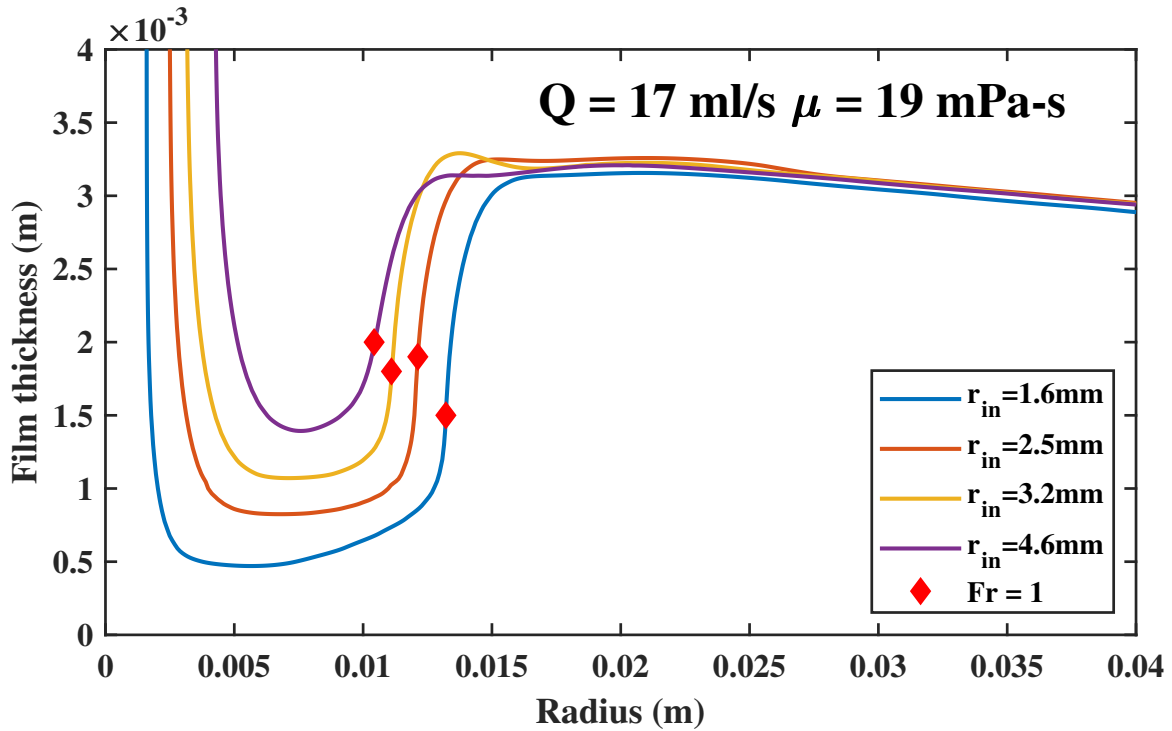


Fig. 2.14 Effect of initial momentum flux on jump radius; radius of inlet has been varied from 1.6mm to 4.6mm to alter the momentum flux. Flow rate, viscosity, and nozzle to disk distance has been kept fixed to 17ml/s 19mPa-s and 8mm respectively

Table 2.7 Comparison of jump radius for various nozzle radii for flow rate of 17 ml/s, dynamic viscosity of 19 mPa-s, nozzle to disk distance is 8 mm and disc radius is 120 mm.

Nozzle radius(m)	Jump radius(m)	Increase(%)
4.6×10^{-3}	10.4×10^{-3}	base case
3.2×10^{-3}	11.1×10^{-3}	6.73
2.5×10^{-3}	12.2×10^{-3}	16.35
1.6×10^{-3}	13.2×10^{-3}	26.92

As depicted by the fig2.14 we can see that initial film thickness is strongly dependent on the selection of the jet inlet radius. As we decrease the nozzle radius we observe a reduction in the initial film thickness. This reduction in film thickness is responsible to increase the initial Froude number (see fig 2.15) which delays the jump and hence we get an increased jump-radius.

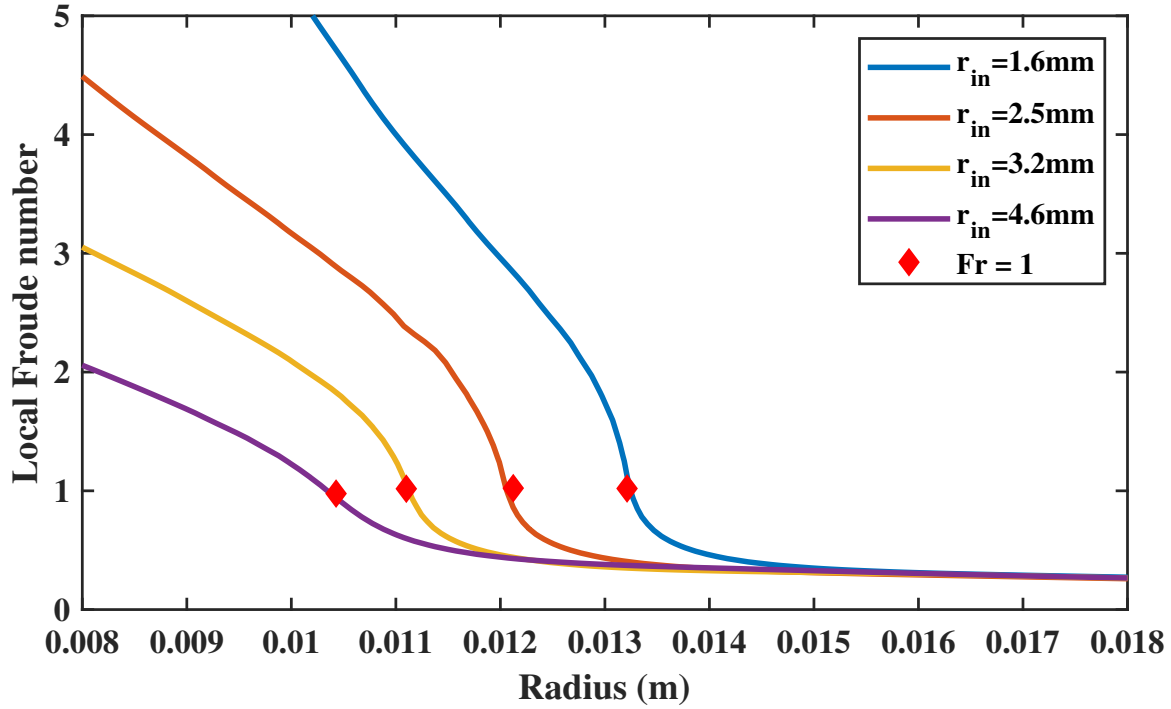


Fig. 2.15 Effect of initial momentum flux on jump radius. Local Froude number has been monitored by changing the nozzle radii from 1.6mm to 4.6mm. Flow rate, viscosity, and nozzle to disk distance has been kept fixed to 17ml/s 19mPa-s and 8mm respectively

2.7.6 Effect of inclination

Understanding effect of body forces such as gravity on the hydraulic jump front is a question of fundamental importance as also point by Duchesne and Limat (2022) in their recent paper. To study this problem we have performed numerical simulations for inclination of 1° , 5° , and 10° from the horizontal. Simulation results shows an increase in jump radius with a decrease in film thickness. This trend is common for both upstream and downstream of hydraulic jump in comparison with the base case of 0° inclination. Due to the inclination, the surface gets converted from a plate to a cone. This change in geometry bring an addition increase in the area for fluid to spread. This feature brings an advantage to both the regimes of flow. For the supercritical regime, an increase surface area caused fluid to flow faster as it spread quicker than the base case of 0° inclination. Moreover, the subcritical region which is predominantly driven by the back pressure caused due to a sudden increase in the film thickness after the jump. This region gains an additional acceleration (a component of gravity) due to the inclination. This surplus acceleration acts as an additional driving mechanism, making the flow faster and reducing the pressure after the hydraulic jump. Combining both the effects in the flow regime due to inclination makes the jump move outward (see fig 2.16). We

have observed that with an increase in the angle of inclination, the jump becomes weak i.e. the ratio of film thickness before and after the jump reduces as compared to the case with no inclination, by keeping other parameters fixed. This also suggests that the effect of downstream boundary conditions on the selection of the jump radius becomes weaker as we increase the angle of inclination. We know that determining the film thickness at the edge of the plate is an ill-posed problem, which for some flow becomes crucial to determine (see Mohajer and Li (2015)), this factor plays a substantial role in determining the jump radius. Inclination in the surface could also help to mitigate the cavity mode oscillation as described by Goerlinger et al. (2023) that occurs for sub-millimeter liquid jets at low flow rates. Our study has been limited to lower value of inclination from the horizontal however, if one increase the value of inclination beyond a critical value, there exist a possibility of no hydraulic jump i.e. flow could remain supercritical to the edge of the plate.

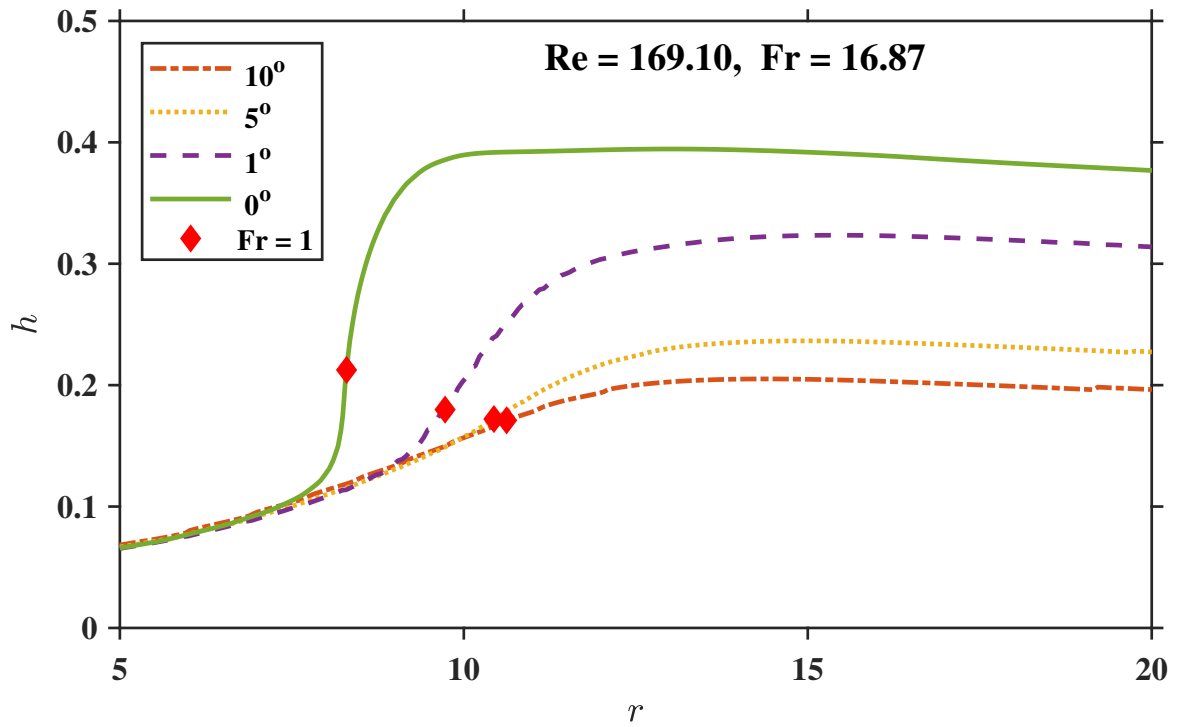


Fig. 2.16 Effect of inclination; Angle of inclination has been varied in the range of 1° to 10° . Numerical simulation has been performed for $Re = 169.10$ and $Fr = 16.87$

2.7.7 Scaling plots

Scaling relation has been developed based on Buckingham-Pi theorem (see sec 2.3) which gives us three different non-dimensional parameters, impingement Reynolds number(Re), impingement Froude number(Fr) and ratio of jump radius to jet radius $\left(\frac{r_j}{r_i}\right)$ [refer Tabel 2.8].

Table 2.8 Definition and ranges for various simulation parameter.

Dimensionless parameter	Minimum value	Maximum value
$Re = \frac{\rho v_{in} r_{in}}{\mu}$	39.21	2164
$Fr = \frac{u_{in}}{(g r_{in})^{1/2}}$	1.2	84.35
θ (degrees)	0°	10°

Assuming the dependence to have a power law nature, we can construct a simple relation between non-dimensional parameters as

$$\frac{r_j}{r_i} = a Re^b Fr^c \quad (2.31)$$

To incorporate the effect of finite size of the disk on the jump-radius Duchesne and Limat (2022) proposed a logarithmic correction. This correction modifies the scaling as follows

$$\frac{r_j}{r_i} = a Re^b Fr^c \ln\left(\frac{r_{edge}}{r_j}\right)^{-1/8} \quad (2.32)$$

where $\ln((r_{edge})(r_j))^{1/8}$ corresponds to the logarithmic correction proposed by Duchesne and Limat (2022), r_{edge} is the radius of the disk, and r_j is the jump-radius. Moreover, to incorporate the effect of the inclination, a factor corresponding to the angle of inclination from the horizontal is proposed. This correction modifies the scaling as follows

$$\frac{r_j}{r_i} = aRe^b Fr^c \ln\left(\frac{r_{edge}}{r_j}\right)^{-1/8} (1 + \sin(\theta))^d \quad (2.33)$$

To determine the exponents of eq. 2.33 *nlinfit* fitting function by MATLAB[®] which provides a least square estimation via an iterative scheme. To estimate the exponent for nonlinear regression an initial value is required which is set to be unity. We estimated the exponent for the scaling using our numerical simulation data and plotted experimental data by Hansen et al. (1997) and found to have a collapse. Moreover, by introducing a logarithmic correction (due to Duchesne and Limat (2022)) we see a better collapse of simulation data even for higher jump-radius as it accounts for the role of finite disk size on jump-radius. However, when we plot the experimental data by Vishwanath et al. (2015) (see Fig 2.20) we obtain very similar slope for both but, there is a systematic offset in the plot. This trend could be due to variations in the film thickness at the edge of the disk as the balance between various forces at the edge will be unique for each liquid. This difference has already been pointed out by Duchesne et al. (2014). They have incorporated an adhoc argument for the film thickness at the edge of the disk corresponding to the capillary-gravity length scale. As already mentioned, the determination of film thickness is an ill-posed problem hence resolving this issue has been kept for future considerations. For the case of circular hydraulic jump on the surface of a cone with mild inclination from the horizontal, we have observed an increase in jump-radius with increasing inclination angle. Fig 2.21 shows a systematic shift in the data for flat and inclined hydraulic jump cases. This trend helped us deduce a generalized scaling relation based on the available energy at the jump-radius which includes the effect of inclination. This excess available energy brings a pre-factor of $1 + \sin(\theta)$ to the excess potential energy for case due to inclination. By introducing an additional inclination factor we obtain a collapse for mild range of inclination (0° to 10°).

2.7.8 Conclusion

Numerical simulations were conducted over an expanded parameter range for circular hydraulic jumps to explore the influence of momentum flux on jump radius (see Table 2.8). The variation in momentum flux was achieved by adjusting the nozzle jet radius while maintaining constant flow rate and impinging height (see Figure 2.13). Additionally, simulations were performed to examine the impact of surface tension on jump radius, revealing its negligible effect under typical terrestrial gravity conditions. However, surface tension may play a crucial role in low-gravity environments (Bhagat and Linden, 2020,

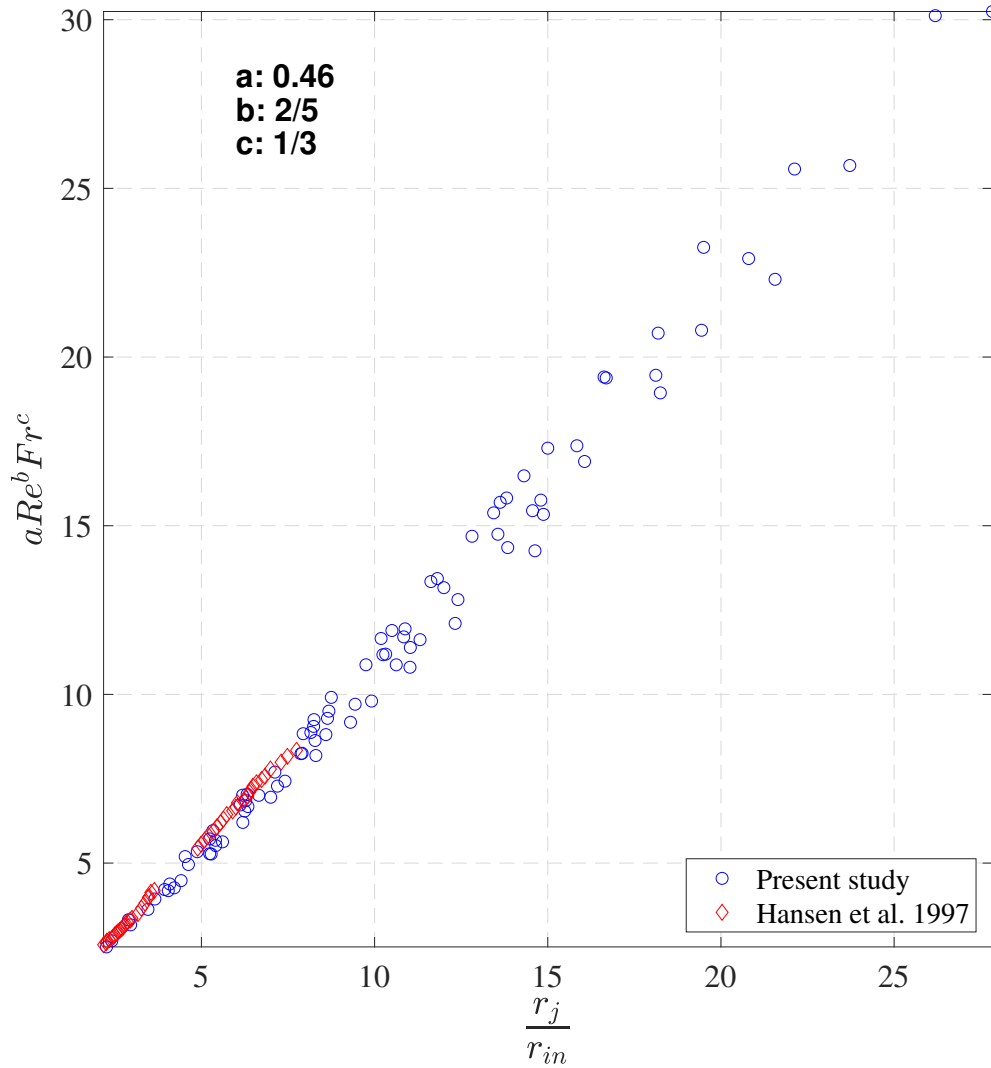


Fig. 2.17 Comparison of numerical simulation and experiments by Hansen et al. (1997); Numerical simulations were performed for dimensionless parameter as presented in Table 2.8

Avedisian and Zhao, 2000). To investigate the effect of inclination of impacting surface to the horizontal (see Figure 2.2), numerical simulations were carried out varying inclination angle from 0° to 10° . Increasing the inclination resulted in an increase of jump radius and a reduction in post-jump film thickness due to decreased back pressure at the jump location (see Figure 2.16). Simulations by varying the disk size indicated a decrease in jump radius and an increase in post-jump film thickness with larger disk radii. A scaling function, derived from Buckingham-Pi analysis and adjusted for finite disk size and inclination, was proposed. This scaling function aligned well with previous experimental findings and successfully accounted for variations even with slight inclinations from the horizontal. Further investigation into the control volume is recommended for future studies to precisely characterize the jump structure.

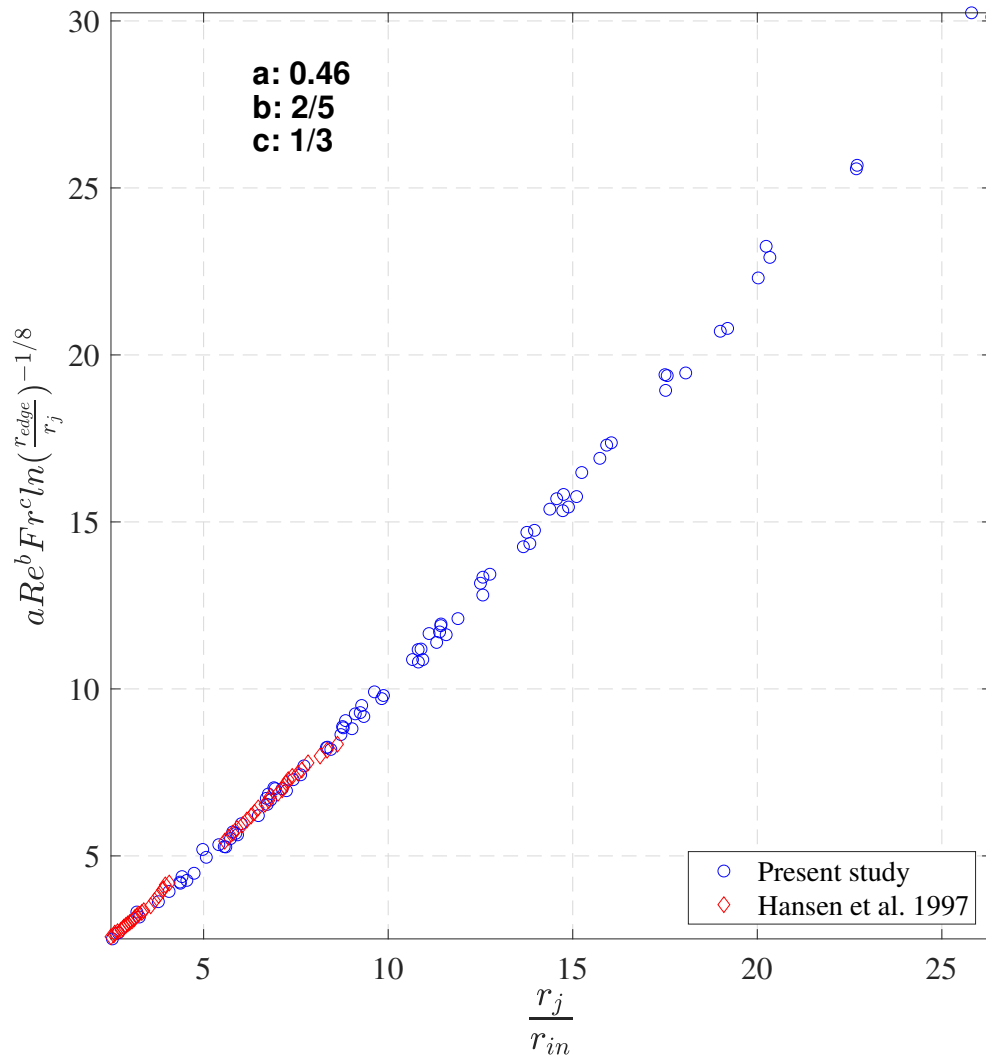


Fig. 2.18 Comparison of numerical simulation and experiments with logarithmic correction proposed by Duchesne and Limat (2022); Numerical simulations were performed for dimensionless parameter as presented in Table 2.8

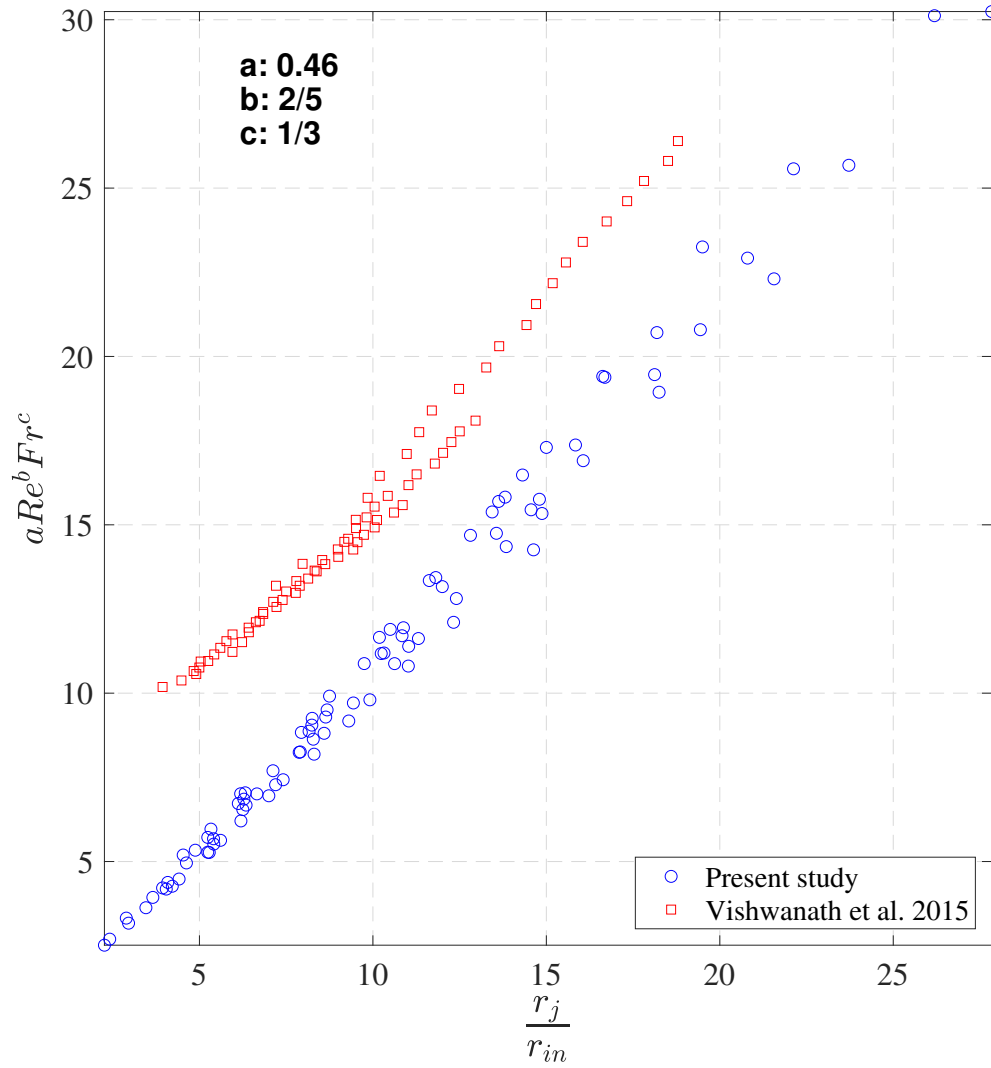


Fig. 2.19 Comparison of numerical simulation and experiments by Vishwanath et al. Vishwanath et al. (2015); Numerical simulations were performed for dimensionless parameter as presented in Table 2.8

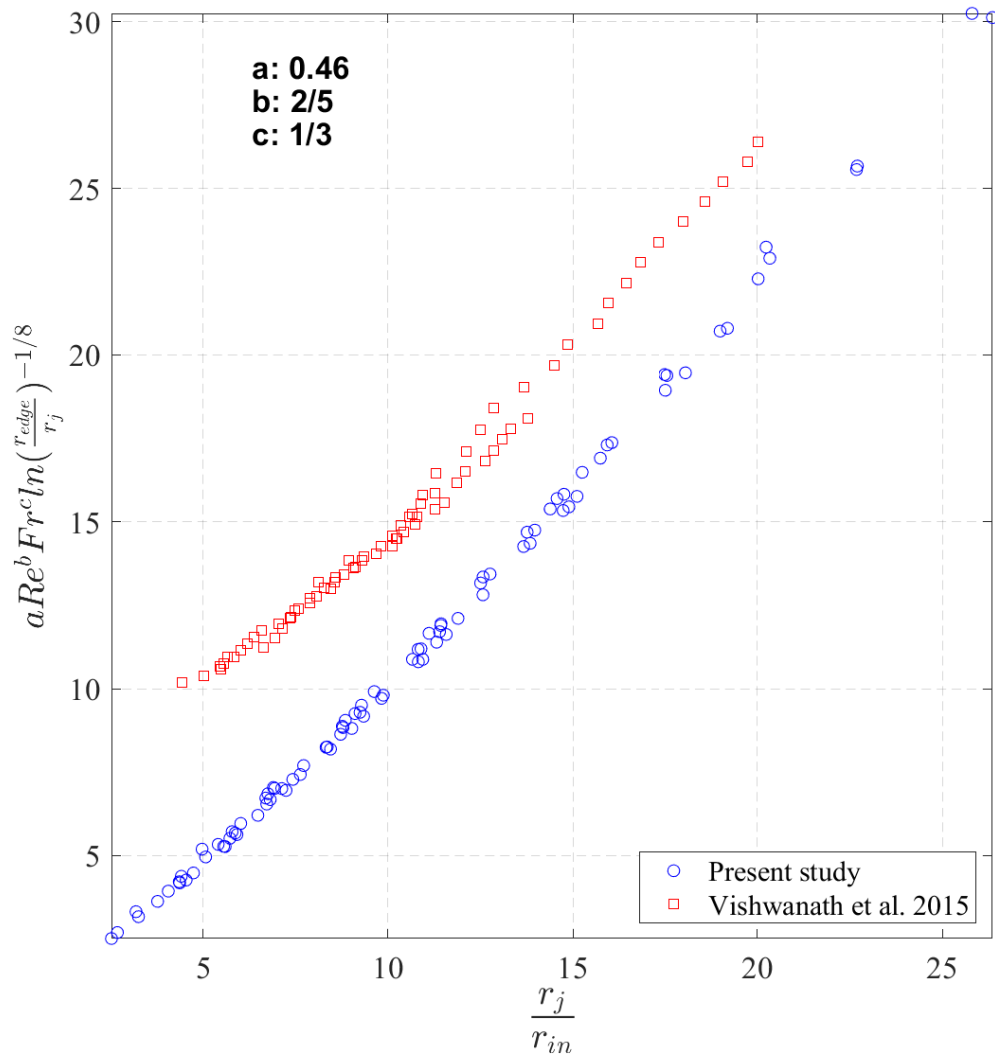


Fig. 2.20 Comparison of numerical simulation and experiments by Vishwanath et al. Vishwanath et al. (2015) with logarithmic correction; Numerical simulations were performed for dimensionless parameter as presented in Table 2.8

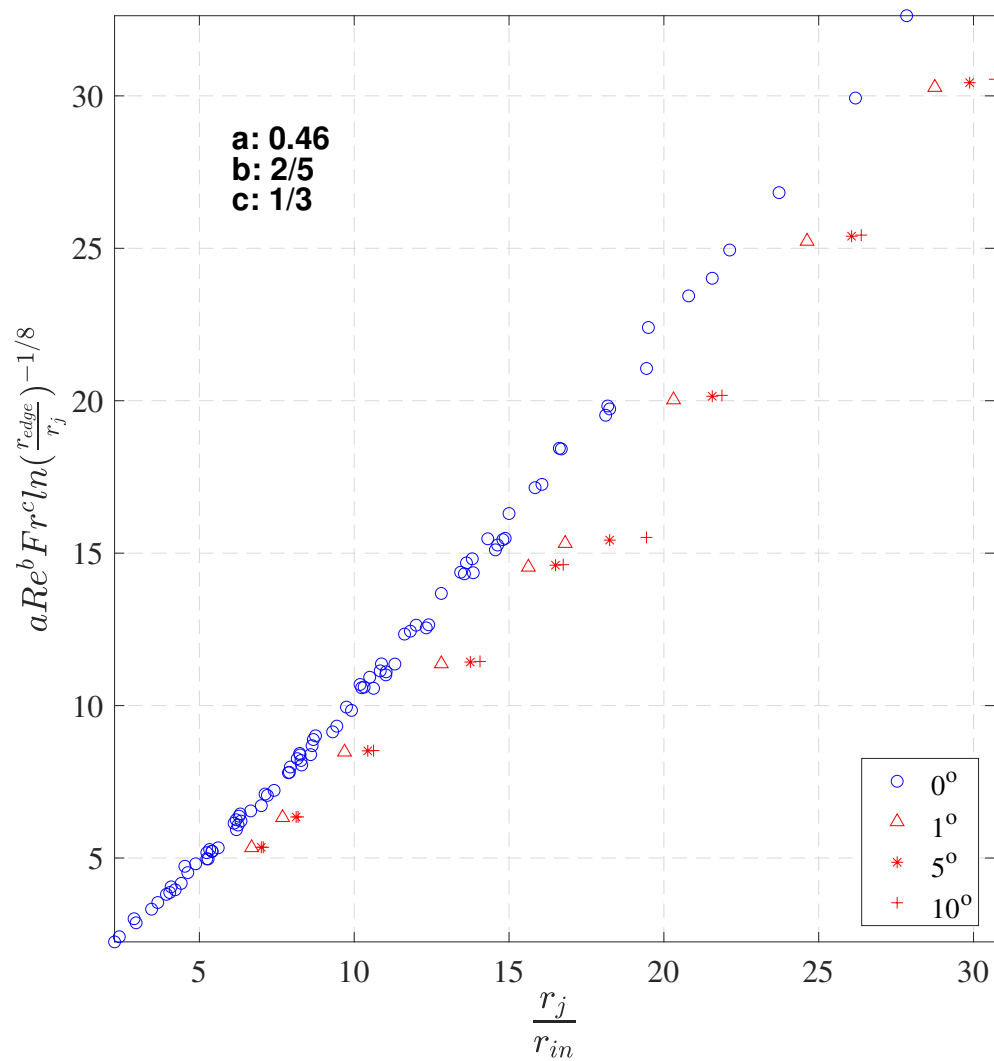


Fig. 2.21 Comparison of numerical simulations with various inclinations with logarithmic correction; Numerical simulations were performed for dimensionless parameter as presented in Table 2.8 with inclination variation in range of 1° to 10°

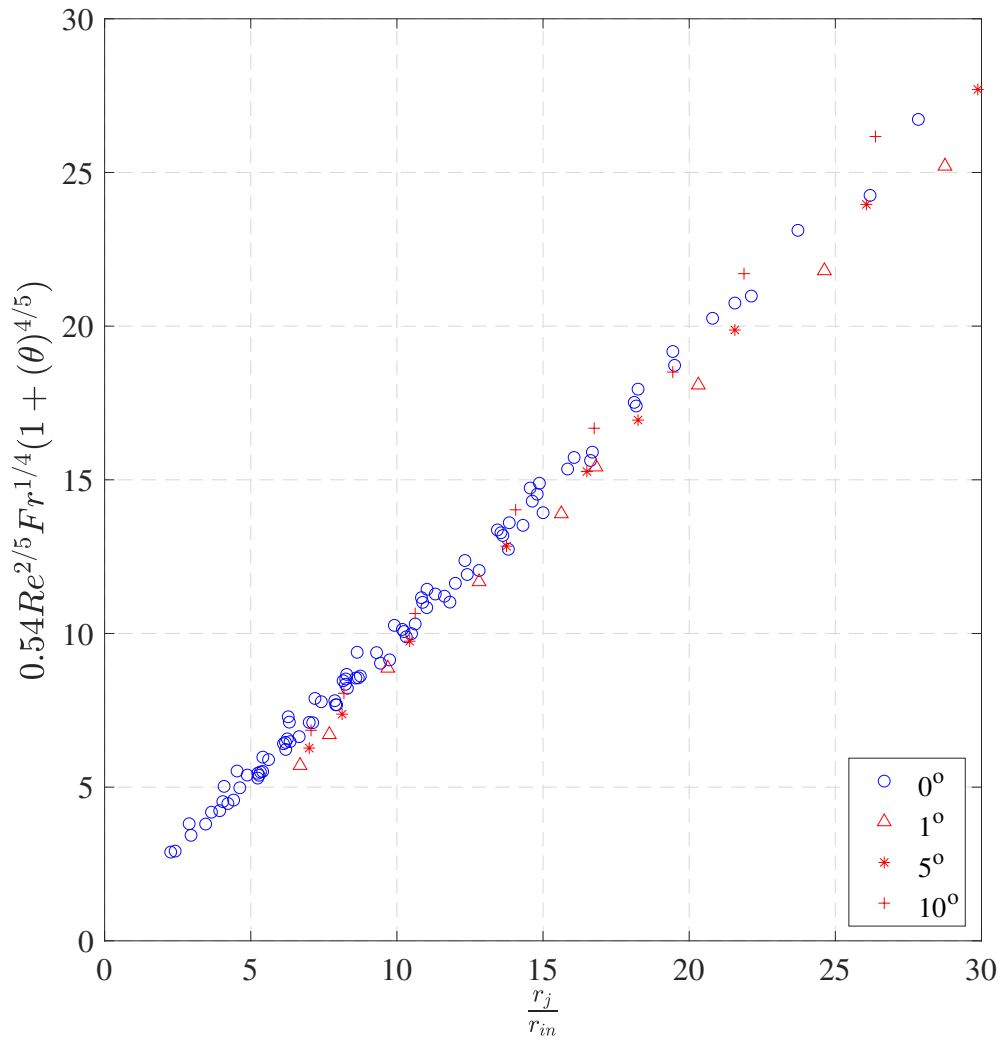


Fig. 2.22 Collapse of non-dimensional jump radius with scaling relation with an inclination factor and logarithmic correction in jump-radius; Numerical simulations were performed for dimensionless parameter as presented in Table 2.8 with inclination variation in range of 1° to 10°

Chapter 3

Optical reconstruction of free surface profile for circular hydraulic jump

3.1 Introduction

Hydraulic jump involves a free surface flow where precise measurement of film thickness is critical for industrial processes like film coating and heat transfer assessment. Previous studies, such as those by Vishwanath et al. (2015), have used intrusive methods to estimate film thickness. In this chapter, we present an optical approach for obtaining instantaneous, non-intrusive measurements of film thickness. Specifically, promising techniques include Digital Fringe Projection (DFP) and Free Surface Synthetic Schlieren (FS-SS) techniques. Optical methods for this application can be classified into three main categories (van Meerkerk et al. (2020) and Gomit et al. (2022)):

- Techniques based on stereo-correlation and key factors at the interface.
- Techniques using fringe projection or patterned projections.
- Techniques that leverage the optical properties (refraction, reflection, and absorption) of light at the gas-liquid interface.

In our experiments, we employed a method based on the apparent displacement of a random dot pattern placed beneath the glass plate over which the hydraulic jump occurs. This technique, initially introduced by Kurata et al. (1990), utilizes the refraction of a grating pattern. Subsequent developments by Tanaka et al. (2000) and Moisy et al. (2009) incorporated random patterns and image correlation methods to estimate the displacement field by comparing images of the distorted and undistorted states, formed with and without film flow respectively.

We specifically adopted the method proposed by Moisy et al. (2009). Our experimental setup was designed to minimize paraxial effects and maintain a weak slope and amplitude approximation. These conditions are crucial for deriving a simplified relationship between the displacement field and the surface gradient, as given by:

$$\nabla h = \frac{-\delta r}{(1 - \eta_r)h_p} \quad (3.1)$$

where ∇h represent the gradient of the film thickness, δr is the displacement of the random dot pattern, η_r is refractive index of air-water interface, and h_p is the distance between liquid-gas interface and random dot pattern.

The method enables the optical reconstruction of the variation of thin film profile for a circular hydraulic jump, a capability not used earlier for this flow. This technique results in reconstruction of the variation of the film thickness along the radial direction of the flow. The experimental procedure requires capturing a set of images of random dot-pattern placed below the glass plate: one with the film flow (distorted) and one without (reference, undistorted). A Digital Image Correlation (DIC) algorithm is then applied to these images to determine the displacement field (δ_r). The approach developed by Moisy et al. (2009) links this displacement field to the gradient of the film thickness.

With the gradient of the height field determined, an integration scheme is used to reconstruct the height profile by estimating the film thickness at a single radial location. This estimate, based on the theory by Watson (1964), serves as the initial condition for the integration, leading to the unique determination of the thickness profile.

3.2 DIC Algorithm

Digital Image Correlation (DIC) is a versatile technique widely employed across various fields, including pattern recognition and fluid mechanics, where it is central to Particle Image Velocimetry (PIV) and particle tracking methods for measuring instantaneous velocity fields. DIC is also a trusted experimental approach for examining the behavior and mechanics of both rigid and deformable bodies under different loading conditions (Peters et al. (1983), Chu et al. (1985), Sutton et al. (1992)). As previously mentioned, DIC involves comparing a set of undistorted (reference, without flow) and distorted (with film flow) image frames. The dot patterns in these images are divided into subdomains, or interrogation windows, and analyzed using cross-correlation algorithms to determine the local displacement of the dot-pattern. In our experiments for extracting displacement fields, we utilize the MATLAB[®] Basic DIC/PIV toolkit developed by Wildeman (2018).

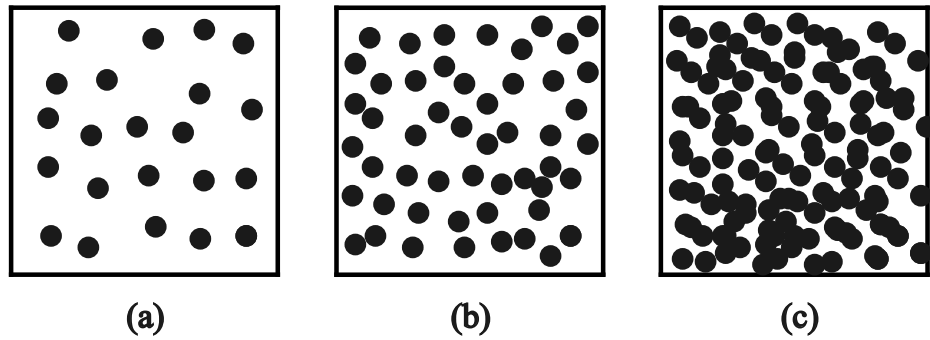


Fig. 3.1 Various types of pattern based on density of random dots; (a) low density random dot pattern; (b) just right density of random dot pattern ($\approx 50\%$ filled area); (c) high density random dot pattern

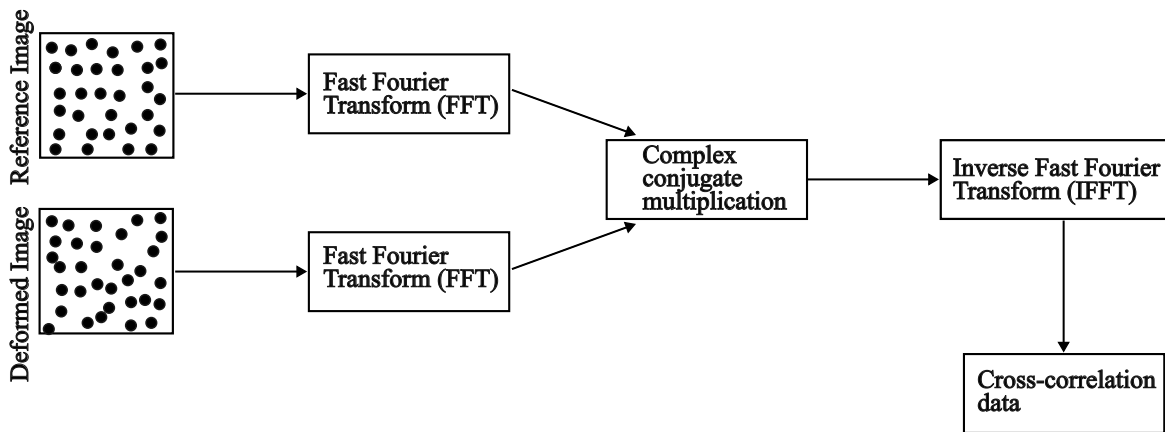


Fig. 3.2 Flow chart for cross-correlation algorithm.

3.2.1 Problems in DIC

- Aperture problem; In practice, it is not possible to map the correspondence of a single pixel in the reference image to the current image, in principle the gray value of a single pixel in the reference image can be found at several different locations in the current image.
- Correspondence problem
- To solve the aperture and correspondence problem surface texture should be isotropic (no preferred orientation) and non-periodic. Speckle patterns can serve as a solution for the non-uniqueness in image matching. Speckle patterns come with additional advantages such as high information content, and also permit us to use smaller aperture (commonly known as subset or window) for pattern matching.

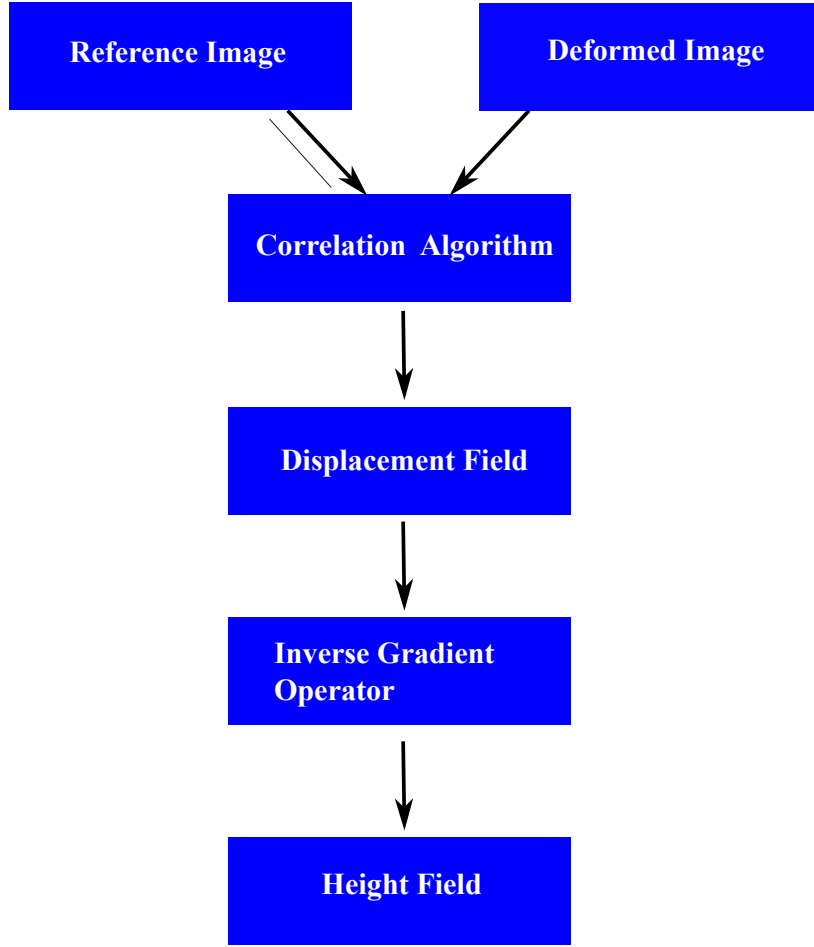


Fig. 3.3 Flow chart for optical reconstruction.

3.2.2 Correlation criteria

Normalized cross-correlation is used

$$C_{CC} = \frac{\sum_{(i,j \in S)} (f(\tilde{x}_{ref}, \tilde{y}_{ref}) - f_m)(g(\tilde{x}_{curr}, \tilde{y}_{curr}) - g_m)}{\sqrt{\sum_{(i,j \in S)} (f(\tilde{x}_{ref}, \tilde{y}_{ref}) - f_m)^2 \sum_{(i,j \in S)} (g(\tilde{x}_{curr}, \tilde{y}_{curr}) - g_m)^2}} \quad (3.2)$$

where f and g are gray scale intensity of reference and current images. f_m and g_m are the mean of gray scale intensity defines as

$$f_m = \frac{\sum_{(i,j \in S)} (f(\tilde{x}_{ref}, \tilde{y}_{ref}))}{n(S)} \quad (3.3)$$

$$f_m = \frac{\sum_{(i,j \in S)} (g(\tilde{x}_{curr}, \tilde{y}_{curr}))}{n(S)} \quad (3.4)$$

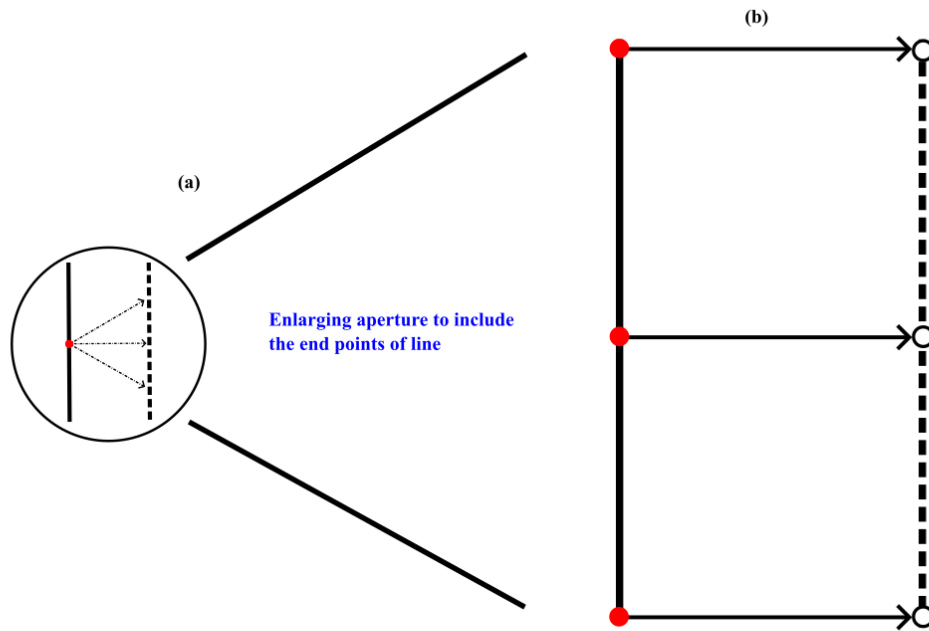


Fig. 3.4 Aperture problem in image matching; (a) A point on a line can be arbitrarily matched to non-unique points on the displaced line. (b) When the aperture is enlarged to include the endpoints of a line, one could achieve a unique matching.

where $n(S)$ is number of points in subset S

3.3 Error quantifiaction

There are various kinds of error (see fig.3.5) that are encountered while performing digital image correlation based on the subset size. Correlation error reduces as we increase the subset size, as the algorithm has now a bigger area for template matching, this increases the chance of finding an appropriate match even for large displacements. On the other hand increase in subset size increases the error because numerical operations are prone to larger and larger discratisation errors. Due to these complications, one has to cautiously decide the right size of subset for DIC based on the lowest amount to total error to generate a faithful displacement field (see fig.3.6).

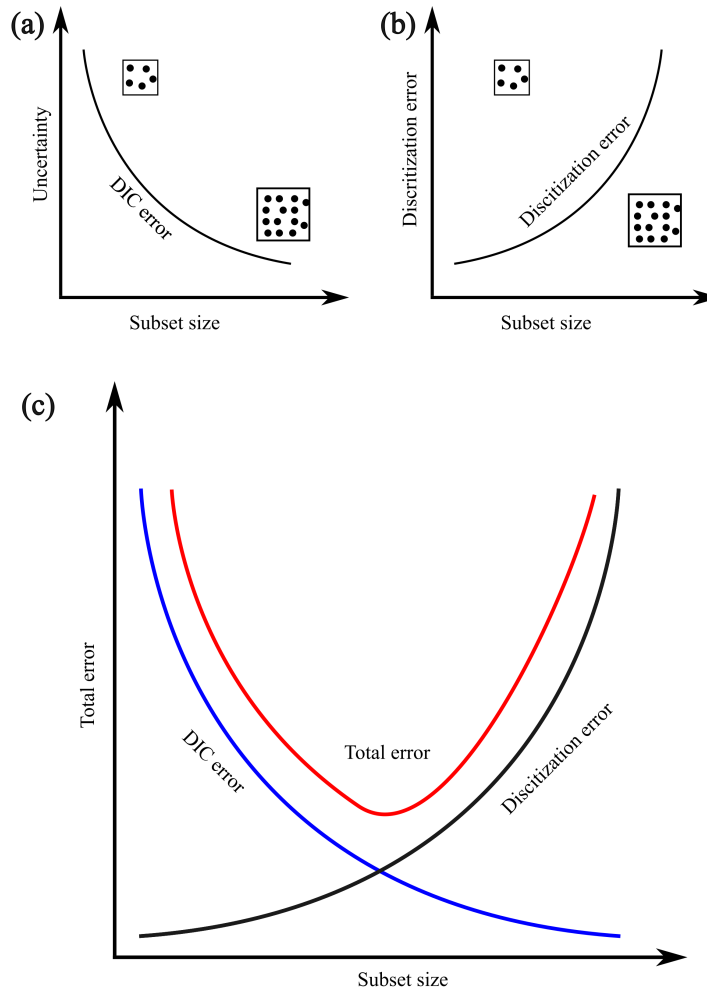


Fig. 3.5 Various types of error in DIC; (a) Uncertainty in measurement; (b) Discretization error; (c) Total error

3.4 Experimental Procedure

3.4.1 Reconstruction of plano-convex lens

Experiments were performed on a glass plate of 300mm diameter and 12.5mm thickness which is subject to a random dot pattern of 0.6mm dot size. The random dot pattern was printed on the Overhead transparency sheet(OHP) covering approximately 50% of the total imaged area. Random dot pattern is illuminated by a non-fluctuating diffuse light source from the bottom. Image is captured from NIKON D5200 camera equipped with a telephoto zoom lens (Nikon AF Nikkor ED 80-200 F2.8). For validation of FS-SS scheme, we

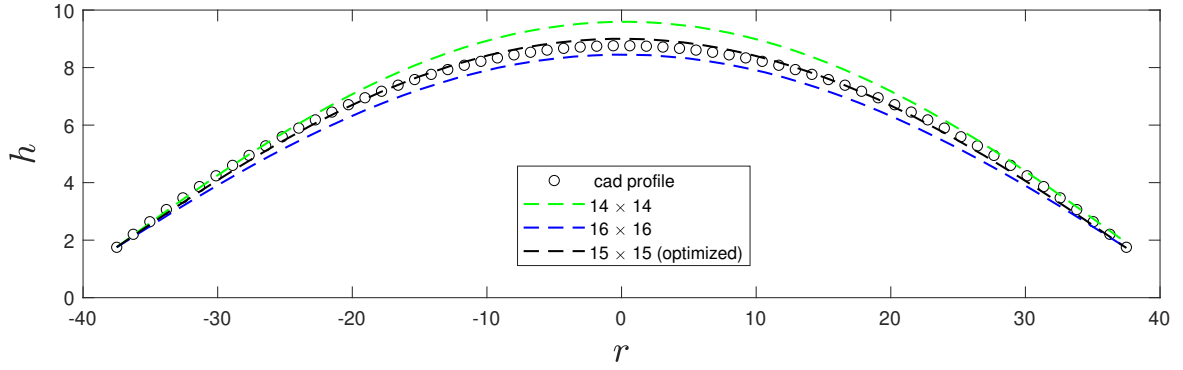


Fig. 3.6 Error in the measurement of profile of plano-convex lens as a function of subset size. Three subset size has been chosen and comparison with the actual profile is depicted

initiated an experiment to determine the free surface profile of a plano-convex lens which is provided by Edmund Optics[®] (75.0 mm Dia \times 200.0 mm FL, Uncoated, Plano-Convex Lens). A set of images were captured to obtain the apparent displacement of the random dot pattern due to the presence of differences in the refractive index (air-glass interface) and curvature of the lens. To reduce the paraxial angle, camera has been placed at a height of 1700 mm above the random dot pattern. The imaged area is 75 mm \times 75 mm which covers the entire area of apparent displacement due to the lens. Images captured for the Digital image correlation had a resolution of 2552px \times 2552px, and a final subset size of 15 px was selected corresponding to a minimum total error(see fig3.11). Images were processed using BASIC PIV/DIC toolkit provided by MATLAB[®] which was developed by Wildeman (2018). The maximum paraxial angle $\beta_{max} = \frac{L}{\sqrt{2}H} = 1.83 \times 10^{-3}$ is within the approximations of the method used for reconstruction. Once the final displacement field is obtained via DIC, a numerical integration needs to be performed. The integration requires computation of inverse gradient, ∇^{-1} which is performed using invgrad MATLAB[®] function which is developed by D'Errico (2013). Profile reconstruction is also sensitive to the vibration present in the system, to overcome this issue experimental setup is supported by rubberized support/legs.

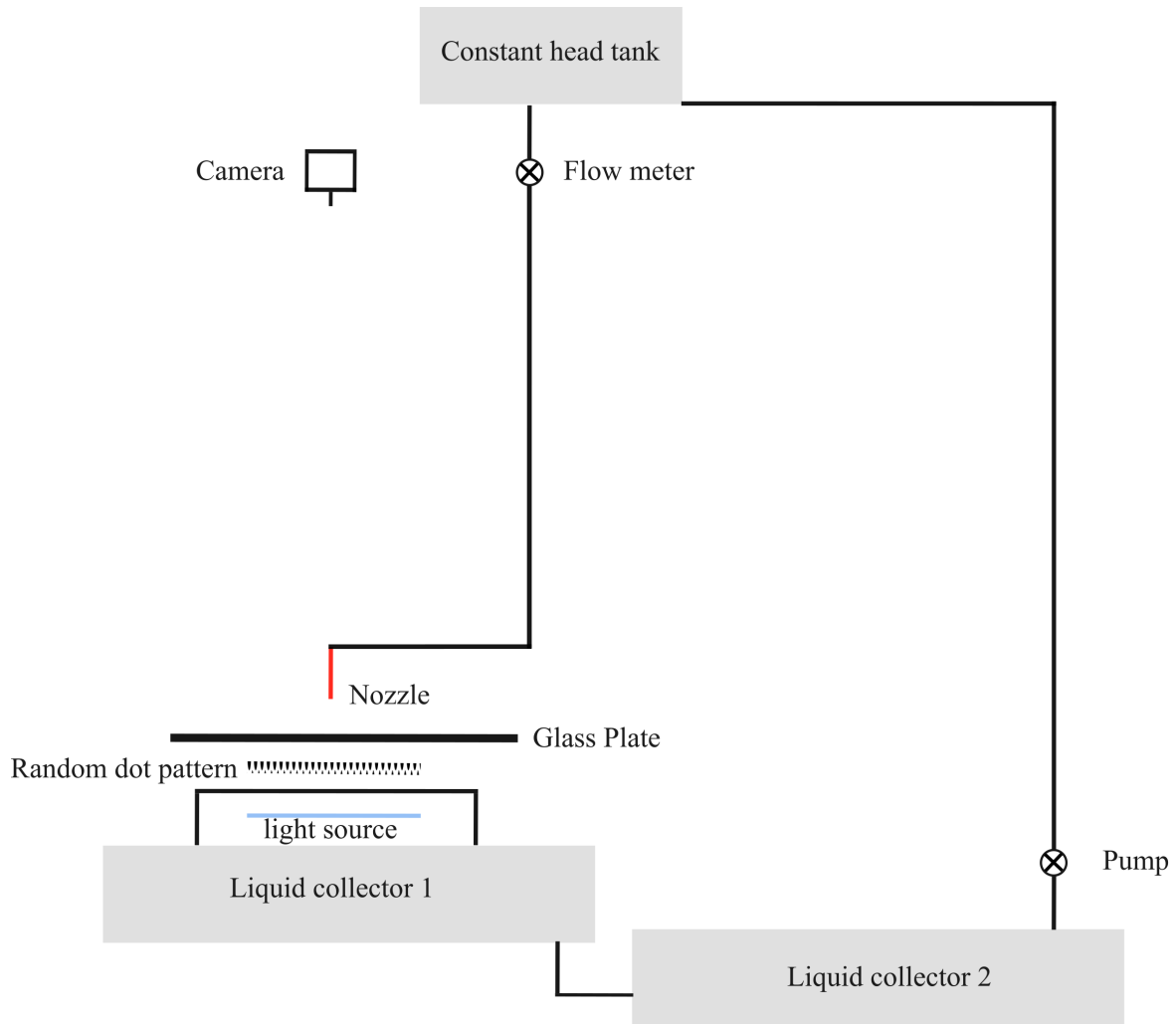


Fig. 3.7 Schematic representation of experimental setup

To validate the method, we performed experiments to obtain a reconstruction of plano-convex lens by Edmund Optics[®] (75.0 mm Dia \times 200.0 mm FL, Uncoated, Plano-Convex Lens). To obtain the exact profile of the lens a CAD file is downloaded from official Edmund Optics[®] website and is compared against the optically reconstructed profile. Error for the system is defined as

$$error(\%) = \frac{|h_{cad} - h_{FS-SS}|}{h_{cad}} \times 100 \quad (3.5)$$

and found to be within 5% error in the profile (see fig 3.9).

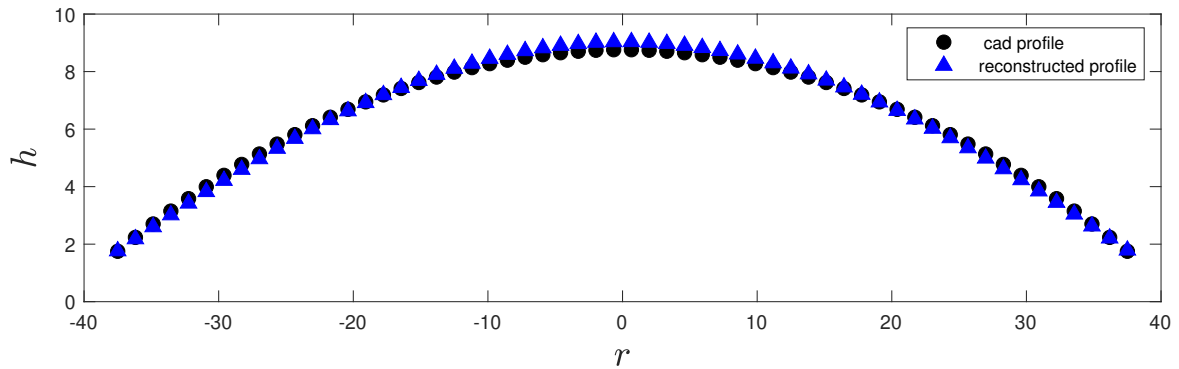


Fig. 3.8 Free surface profile along with gradient of height profile and error in estimation of reconstructed height profile

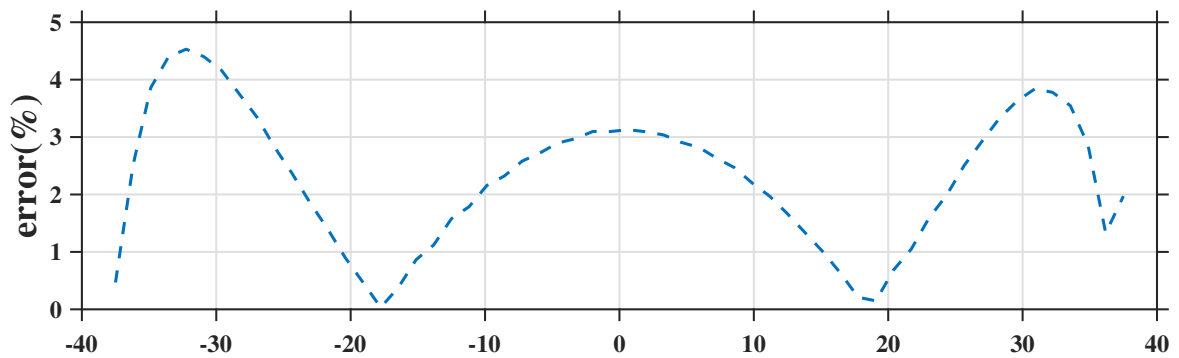


Fig. 3.9 Error obtained in the reconstructed profile of plano-convex lens according to eq 3.5.

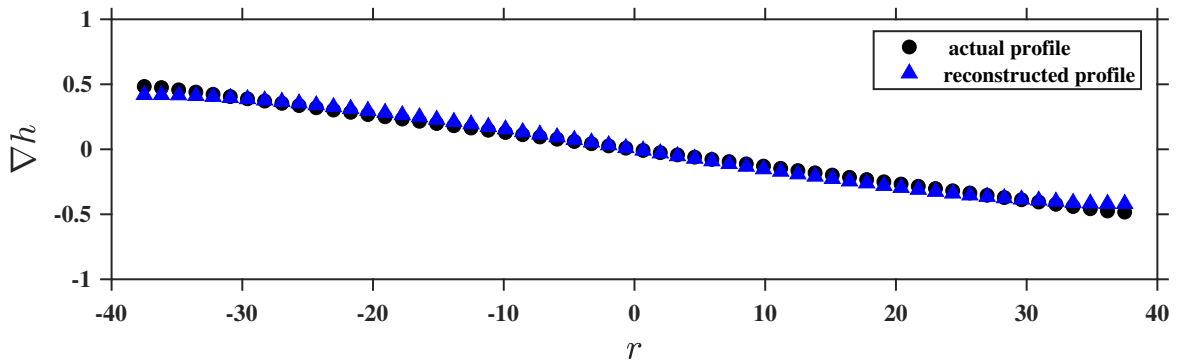


Fig. 3.10 Comparison of gradient obtained by optical reconstruction to the CAD profile

3.4.2 Reconstruction of CHJ

Experiments were conducted using a 300 mm diameter glass plate with a 12.5 mm thickness and chamfered edges. The nozzle diameter was set at 9 mm, and the jet impingement height was fixed at 50 mm. Flow rates tested were 45, 60, and 90 LPH. A flow meter, attached to a constant head setup with a valve, controlled the flow rates. The constant head tank

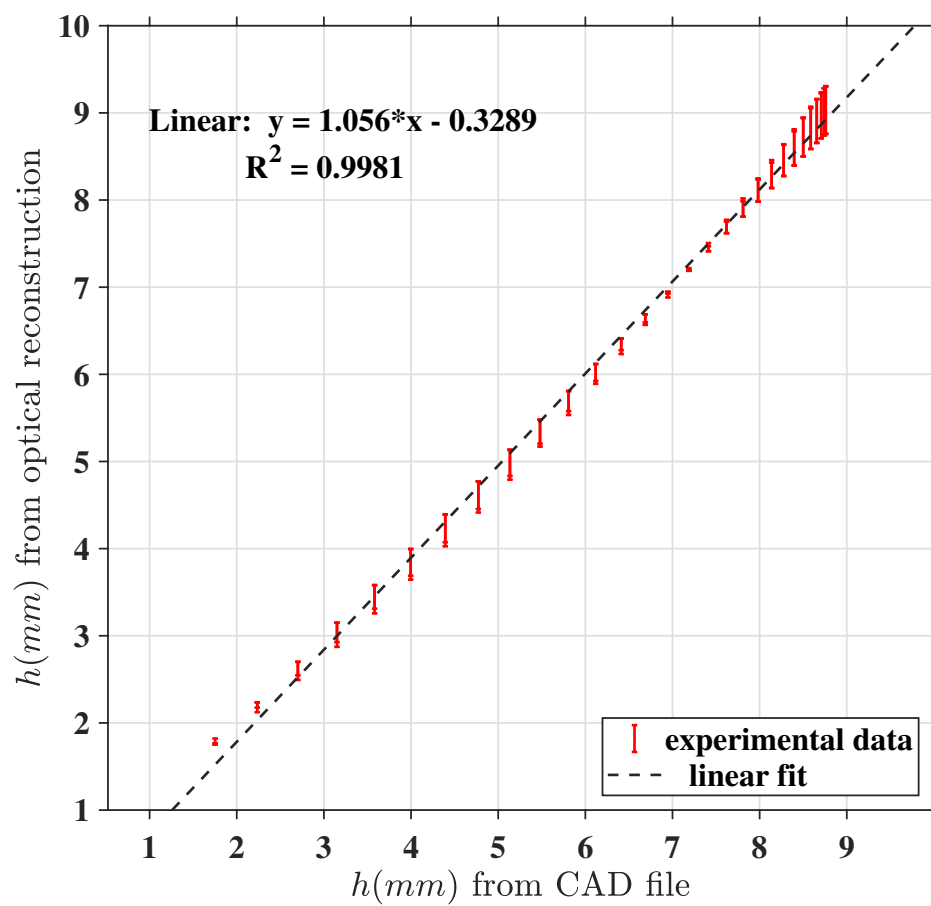


Fig. 3.11 Free surface error in the estimation of reconstructed height profile compared with the actual profile obtained by CAD file.

was positioned 1700 mm above the glass plate to ensure a sufficient head to maintain the desired flow rates. Water runoff from the glass plate's edges was collected in a primary water collector, then transferred to a secondary water collector through a passage (see fig 3.7). A pump in the secondary collector recirculated the water back to the constant head setup.

Images were captured using a NIKON D5200 camera equipped with a Nikon AF Nikkor ED 80-200 F2.8 telephoto lens. A random dot pattern with a 0.6 mm dot size was created using the PIVmat toolbox in MATLAB[®] via the makebospattern.m function. This pattern was printed on an Overhead Projector (OHP) sheet and placed below the glass plate, illuminated from below with diffuse light. Images were taken from a height of 1700 mm to reduce parallax errors. Digital image correlation was performed on pairs of reference and deformed images to obtain the displacement field using the MATLAB[®] Basic PIV/DIC toolkit developed by S. Wildemann.

We applied the Free Surface Synthetic Schlieren (FS-SS) framework from Moisy et al. (2009), which connects the apparent displacement of the random dot pattern to the gradient of liquid film thickness as described by equation 3.1. To obtain the exact height field, numerical integration was carried out using the scheme provided by D'Errico (2013). To determine the constant of integration, the height of the liquid film at a specific point in the flow field was needed. This was estimated using the boundary layer theory before the hydraulic jump, as originally developed by Watson (1964) (see eq.24, eq.37, and eq.39 in the paper). Upon jet impingement on the solid surface, an initial inviscid spread is observed, followed by the development of the boundary layer from the center of impingement (see fig3.12). Initially, the film thickness decreases due to the inviscid spread, but as the boundary layer reaches the free surface, viscosity causes the film thickness to increase. Watson (1964) provided an expression to estimate the radial distance from the center of impingement where the boundary layer meets the free surface and the film thickness is minimized, based on flow rate, liquid viscosity, and jet radius at the point of impingement. This estimated height at that radius was used as the initial condition for integration.

$$r_0 = 2^{-1/3}b \quad (3.6)$$

$$h_0 = \frac{2^{1/3}\pi^2}{\sqrt{3}} \frac{\nu b^2}{Q} \quad (3.7)$$

$$b^3 = \frac{9\sqrt{3}c(3\sqrt{3}c - \pi)}{16\pi^3} \frac{Qr_{jet}^2}{\nu} \quad (3.8)$$

where $c = 1.402$ is a known constant in the Watson's formulation, ν is kinematic viscosity, Q is the flow rate, and r_{jet} is the radius of the liquid jet at the point of impingement.

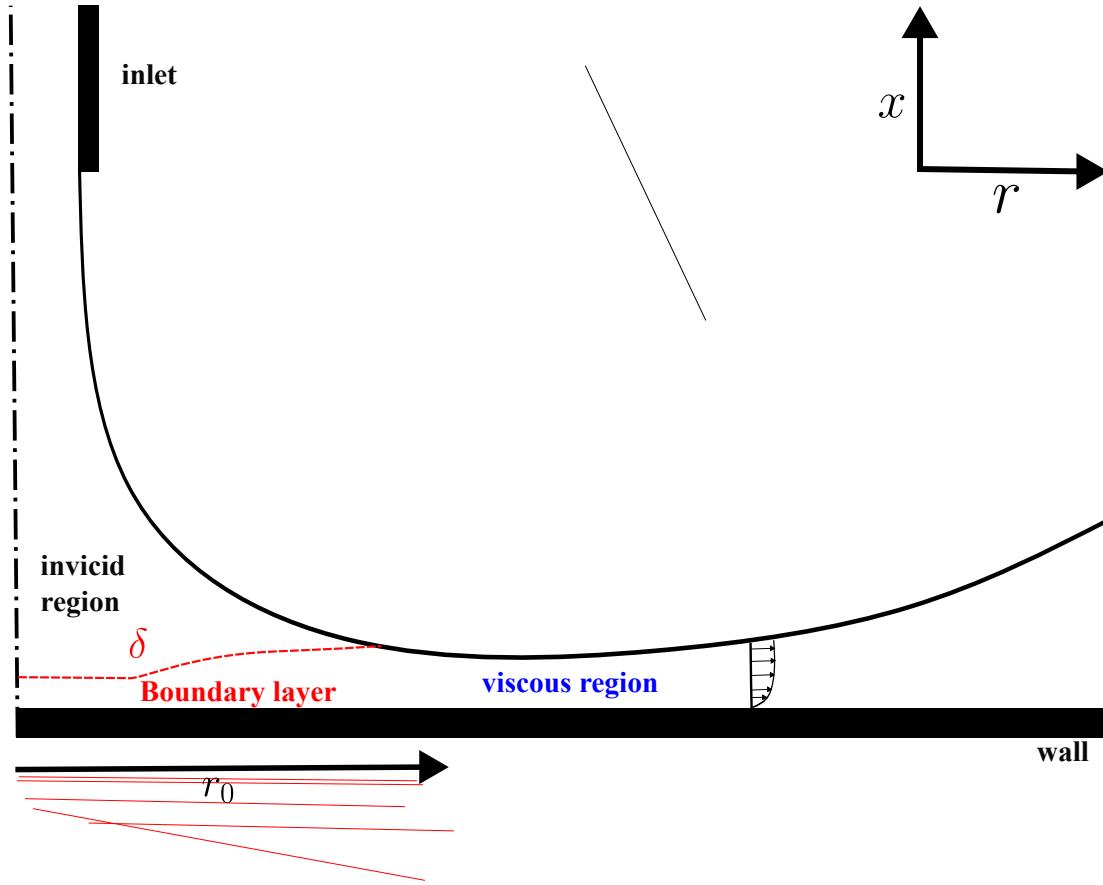


Fig. 3.12 Schematic of various region in liquid film; Growth of the viscous boundary layer begin at the center of impingement and touches the free surface at the radius r_0

3.5 Conclusion and Future direction

In this chapter, we employed the Free Surface Synthetic Schlieren (FS-SS) optical technique to reconstruct the radial variation of film thickness in a circular hydraulic jump. For calibration, we first conducted experiments to reconstruct the profile of a plano-convex lens. With an optimized configuration, we achieved a maximum profile estimation error of less than 5%. After validating the methodology with the plano-convex lens, we use calibrated parameters to estimate the film thickness in the circular hydraulic jump.

We used the Digital Image Correlation (DIC) algorithm to compute the apparent displacement field of a random dot pattern. This displacement field, which correlates with the gradient of the height profile (see Eq.: 3.1), was numerically integrated to determine the film thickness profile. Initial conditions for integrating the gradient field were established using theoretical insights from Watson (1964). The integration, performed using a least-squares formulation,

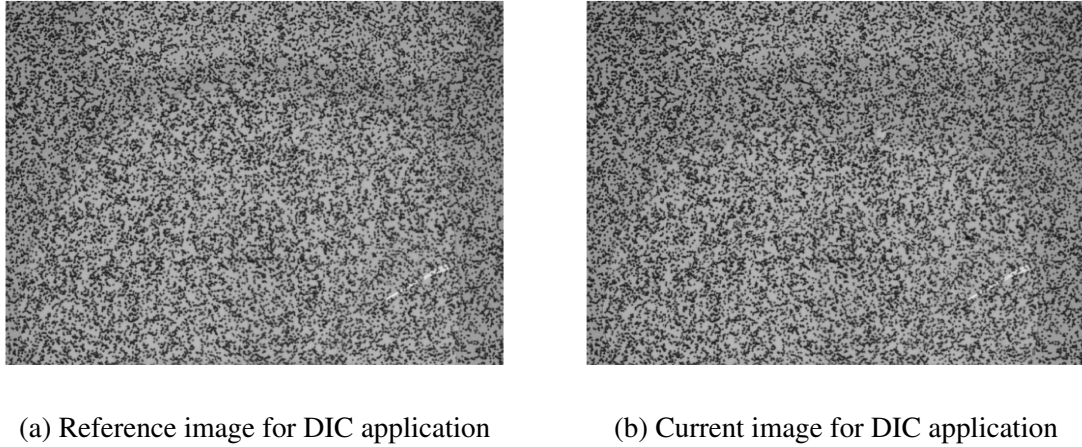


Fig. 3.13 Set of images for performing Digital image correlation of circular hydraulic jump; Experiment was performed at a flow rate of 60 LPH with nozzle diameter of 10 mm and height of impingement to be 100 mm

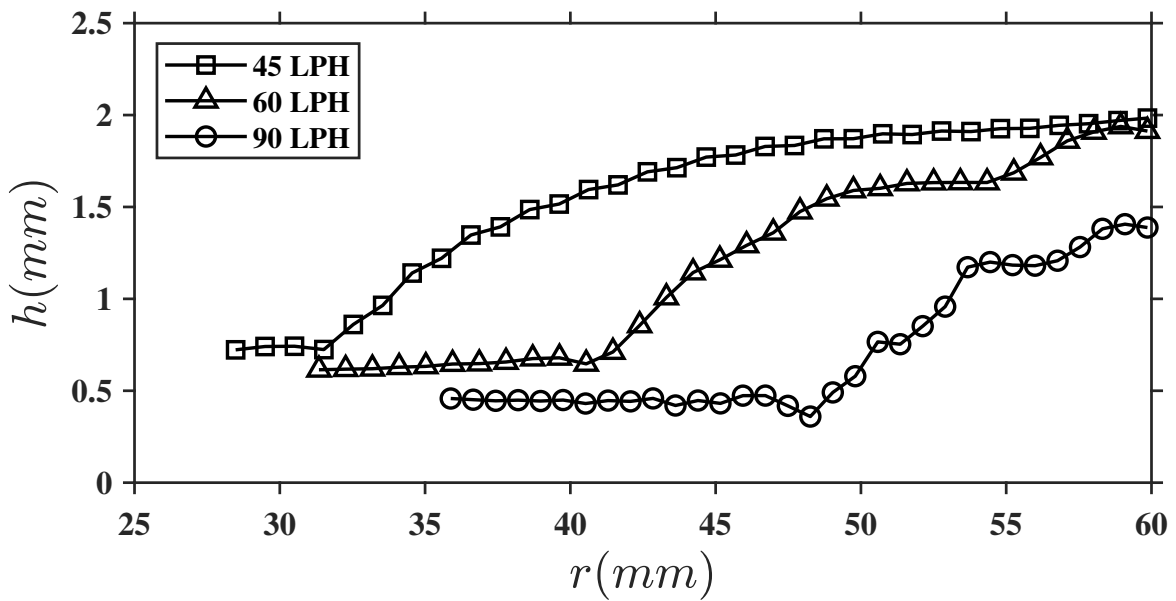


Fig. 3.14 Optically reconstructed free surface profile for circular hydraulic jump. Flow rate of 45,60, and 90 LPH was maintained with a nozzle radius of 9 mm and disk to nozzle distance of 50 mm.

proved to be both accurate and computationally efficient. To minimize parallax error, we positioned the camera at a considerable distance from the dot pattern, and a rubberized base was used to isolate the system from vibrations, further reducing errors. We successfully reconstructed the free surface profiles of circular hydraulic jumps at flow rates of 30 LPH, 45 LPH, and 60 LPH. Future work will explore hydraulic jumps on conical surfaces and

circular hydraulic jumps with non-Newtonian fluids. The current method, which relies on the apparent displacement of a random dot pattern, is limited to transparent liquids. For opaque liquids such as paints, techniques like digital fringe projection (see Zhang (2010)) could be employed.

References

- Avedisian, C. and Zhao, Z. (2000). The circular hydraulic jump in low gravity. *Proceedings of the Royal Society of London. Series A: Mathematical, Physical and Engineering Sciences*, 456(2001):2127–2151.
- Bhagat, R. K., Jha, N., Linden, P., and Wilson, D. I. (2018). On the origin of the circular hydraulic jump in a thin liquid film. *Journal of Fluid Mechanics*, 851:R5.
- Bhagat, R. K. and Linden, P. F. (2020). The circular capillary jump. *Journal of Fluid Mechanics*, 896:A25.
- Bhagat, R. K. and Linden, P. F. (2022). The circular hydraulic jump; the influence of downstream flow on the jump radius. *Physics of Fluids*, 34(7).
- Bohr, T., Dimon, P., and Putkaradze, V. (1993). Shallow-water approach to the circular hydraulic jump. *Journal of Fluid Mechanics*, 254:635–648.
- Brackbill, J. U., Kothe, D. B., and Zemach, C. (1992). A continuum method for modeling surface tension. *Journal of computational physics*, 100(2):335–354.
- Bush, J. W. and Aristoff, J. M. (2003). The influence of surface tension on the circular hydraulic jump. *Journal of Fluid Mechanics*, 489:229–238.
- Bush, J. W., Aristoff, J. M., and Hosoi, A. (2006). An experimental investigation of the stability of the circular hydraulic jump. *Journal of Fluid Mechanics*, 558:33–52.
- Chu, T., Ranson, W., and Sutton, M. A. (1985). Applications of digital-image-correlation techniques to experimental mechanics. *Experimental mechanics*, 25:232–244.
- Craik, A., Latham, R., Fawkes, M., and Gribbon, P. (1981). The circular hydraulic jump. *Journal of Fluid Mechanics*, 112:347–362.
- Dasgupta, R. (2010). *A computational and semi-analytical study of laminar standing hydraulic jumps*. PhD thesis, Jawaharlal Nehru Centre for Advanced Scientific Research.
- D’Errico, J. (2013). Inverse (integrated) gradient. *MathWorks*.
- Duchesne, A., Lebon, L., and Limat, L. (2014). Constant froude number in a circular hydraulic jump and its implication on the jump radius selection. *Europhysics Letters*, 107(5):54002.
- Duchesne, A. and Limat, L. (2022). Circular hydraulic jumps: Where does surface tension matter? *Journal of Fluid Mechanics*, 937:R2.

- Ellegaard, C., Hansen, A. E., Haaning, A., and Bohr, T. (1996). Experimental results on flow separation and transitions in the circular hydraulic jump. *Physica Scripta*, 1996(T67):105.
- Fernandez-Feria, R., Sanmiguel-Rojas, E., and Benilov, E. (2019). On the origin and structure of a stationary circular hydraulic jump. *Physics of Fluids*, 31(7).
- Goerlinger, A., Baudoin, M., Zoueshtiagh, F., and Duchesne, A. (2023). Oscillations and cavity modes in the circular hydraulic jump. *Phys. Rev. Lett.*, 131:194001.
- Gomit, G., Chatellier, L., and David, L. (2022). Free-surface flow measurements by non-intrusive methods: a survey. *Experiments in Fluids*, 63(6):94.
- Haider, J. (2013). Numerical modelling of evaporation and condensation phenomena - numerische modellierung von verdampfungs- und kondensationsphänomenen. Master's thesis, Universität Stuttgart.
- Hansen, S. H., Hørlück, S., Zauner, D., Dimon, P., Ellegaard, C., and Creagh, S. C. (1997). Geometric orbits of surface waves from a circular hydraulic jump. *Phys. Rev. E*, 55:7048–7062.
- Hirt, C. W. and Nichols, B. D. (1981). Volume of fluid (vof) method for the dynamics of free boundaries. *Journal of computational physics*, 39(1):201–225.
- Ipatova, A., Smirnov, K., and Mogilevskiy, E. (2021). Steady circular hydraulic jump on a rotating disk. *Journal of Fluid Mechanics*, 927:A24.
- Kasimov, A. R. (2008). A stationary circular hydraulic jump, the limits of its existence and its gasdynamic analogue. *Journal of Fluid Mechanics*, 601:189–198.
- Kurata, J., Grattan, K., Uchiyama, H., and Tanaka, T. (1990). Water surface measurement in a shallow channel using the transmitted image of a grating. *Review of Scientific Instruments*, 61(2):736–739.
- Liu, X. and Lienhard, J. (1993). The hydraulic jump in circular jet impingement and in other thin liquid films. *Experiments in Fluids*, 15(2):108–116.
- Liu, X., Lienhard, J., and Lombara, J. (1991). Convective heat transfer by impingement of circular liquid jets.
- Mohajer, B. and Li, R. (2015). Circular hydraulic jump on finite surfaces with capillary limit. *Physics of Fluids*, 27(11).
- Moisy, F., Rabaud, M., and Salsac, K. (2009). A synthetic schlieren method for the measurement of the topography of a liquid interface. *Experiments in Fluids*, 46(6):1021–1036.
- Peters, W., Ranson, W., Sutton, M., Chu, T., and Anderson, J. (1983). Application of digital correlation methods to rigid body mechanics. *Optical Engineering*, 22(6):738–742.
- Rayleigh, L. (1914). On the theory of long waves and bores. *Proceedings of the Royal Society of London. Series A, Containing Papers of a Mathematical and Physical Character*, 90(619):324–328.

- Sutton, M., Turner, J., Chao, Y., Bruck, H., and Chae, T. (1992). Experimental investigations of three-dimensional effects near a crack tip using computer vision. *International journal of fracture*, 53:201–228.
- Tanaka, G., Okamoto, K., and Madarame, H. (2000). Experimental investigation on the interaction between polymer solution jet and free surface. *Experiments in Fluids*, 29(2):178–183.
- Tani, I. (1949). Water jump in the boundary layer. *Journal of the Physical Society of Japan*, 4(4-6):212–215.
- Ubbink, O. and Issa, R. (1999). A method for capturing sharp fluid interfaces on arbitrary meshes. *Journal of computational physics*, 153(1):26–50.
- van Meerkerk, M., Poelma, C., and Westerweel, J. (2020). Scanning stereo-plif method for free surface measurements in large 3d domains. *Experiments in Fluids*, 61(1):19.
- Vishwanath, K. P., Dasgupta, R., Govindarajan, R., and Sreenivas, K. R. (2015). The effect of initial momentum flux on the circular hydraulic jump. *Journal of Fluids Engineering*, 137(6):061301.
- Wang, W., Baayoun, A., and Khayat, R. E. (2023). A coherent composite approach for the continuous circular hydraulic jump and vortex structure. *Journal of Fluid Mechanics*, 966:A15.
- Wang, X., Dagan, Z., and Jiji, L. (1989). Heat transfer between a circular free impinging jet and a solid surface with non-uniform wall temperature or wall heat flux—1. solution for the stagnation region. *International journal of heat and mass transfer*, 32(7):1351–1360.
- Wang, Y. and Khayat, R. E. (2019). The role of gravity in the prediction of the circular hydraulic jump radius for high-viscosity liquids. *Journal of Fluid Mechanics*, 862:128–161.
- Wang, Y. and Khayat, R. E. (2021). The effects of gravity and surface tension on the circular hydraulic jump for low- and high-viscosity liquids: A numerical investigation. *Physics of Fluids*, 33(1):012105.
- Watson, E. (1964). The radial spread of a liquid jet over a horizontal plane. *Journal of Fluid Mechanics*, 20(3):481–499.
- Wildeman, S. (2018). Real-time quantitative schlieren imaging by fast fourier demodulation of a checkered backdrop. *Experiments in Fluids*, 59(6):97.
- Yeckel, A. and Middleman, S. (1987). Removal of a viscous film from a rigid plane surface by an impinging liquid jet. *Chemical Engineering Communications*, 50:165–175.
- Zhang, S. (2010). Recent progresses on real-time 3d shape measurement using digital fringe projection techniques. *Optics and lasers in engineering*, 48(2):149–158.
- Zhou, G. and Prosperetti, A. (2022). Hydraulic jump on the surface of a cone. *Journal of fluid mechanics*, 951:A20.

Appendix A

Derivation of viscous axisymmetric spread for subcritical region in the circular hydraulic jump

Assuming the flow after the jump to be unidirectional and steady with lubrication approximation. The pressure in the direction of spread is only function of film thickness, and is constant in direction perpendicular to the spread. One could write continuity and momentum equations as

$$\frac{1}{r} \frac{\partial r v_r}{\partial r} + \frac{\partial v_x}{\partial x} = 0 \quad (\text{A.1})$$

$$\frac{\partial p}{\partial r} = \mu \frac{\partial^2 v_r}{\partial z^2} \quad (\text{A.2})$$

Since we already have assumed pressure to be hydrostatic in nature. We can assume it to have a form $P(r) = \rho g h(r)$ where, ρ is density of fluid, g is acceleration due to gravity, and $h(r)$ is height field as a function of radial spread of thin film. With these assumption we can have a simplified momentum equation as

$$\rho g \frac{\partial h}{\partial r} = \mu \frac{\partial^2 v_r}{\partial z^2} \quad (\text{A.3})$$

We need to solve both continuity and momentum equation using the following boundary conditions.

- No slip and no penetration at wall ($v_r = v_x = 0$ at $x = 0$)
- Stress free boundary at the interface ($\frac{\partial v_r}{\partial x} = 0$ at $x = h(r)$)

Upon integration once eqnA.3 and applying stress free boundary condition at the interface we obtain the following equation

$$\frac{dv_r}{dx} = \frac{g}{\nu} \frac{dh}{dr} x + c \quad (\text{A.4})$$

where value of the constant $c = -\frac{g}{\nu} \frac{dh}{dr} h(x)$.

Substituting the value of integration constant again into eqnA.4 we obtain

$$\frac{dv_r}{dx} = \frac{g}{\nu} \frac{dh}{dr} (x - h(x)) \quad (\text{A.5})$$

Upon integrating eqnA.5 and applying no slip boundary condition at the wall we obtain the following form of the radial velocity function

$$v_r = \frac{g}{\nu} \frac{dh}{dr} (x^2/2 - h(x)x) \quad (\text{A.6})$$

To obtain the average velocity of the flow we integrate A.6 over the film thickness and normalize it with the height at that radial location.

$$U = \frac{1}{h} \int_0^h u_r dx \quad (\text{A.7})$$

Upon integration we obtain

$$U = -\frac{1}{h} \frac{g}{\nu} \frac{dh}{dr} \left(\frac{h^3}{3} \right) \quad (\text{A.8})$$

Substituting average velocity in the flow rate (Q) equation we obtain

$$Q = 2\pi r h U \quad (\text{A.9})$$

$$Q = 2\pi r h \left(-\frac{1}{h} \frac{g}{\nu} \frac{dh}{dr} \left(\frac{h^3}{3} \right) \right) \quad (\text{A.10})$$

rearranging in integrating the above equation with suitable limits we obtain

$$-\frac{3Q\nu}{2\pi g} \int_{r_j}^{r_{edge}} \frac{\partial r}{r} = \int_{H_j}^{H_{edge}} h^3 dh \quad (\text{A.11})$$

upon integration we get the final equation for the height at the jump location based on film thickness at the edge, flow rate, kinematic viscosity, gravity and distance between jump location and the edge of the plate as

$$H_j = H_{edge} + 6 \frac{Qv}{\pi g} \log \frac{r_{edge}}{r_j} \quad (\text{A.12})$$

